

**Dynamic Simulation of Heart Mitral Valve with Transversely Isotropic
Material Model**

by

Eli Weinberg

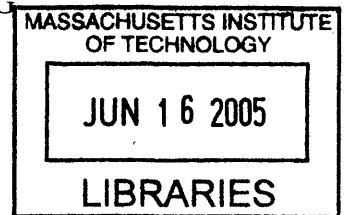
B.S. Mechanical Engineering
Massachusetts Institute of Technology, 2002

SUBMITTED TO THE DEPARTMENT OF MECHANICAL ENGINEERING IN
PARTIAL FULFILLMENT OF THE REQUIREMENTS FOR THE DEGREE OF

MASTER OF SCIENCE IN MECHANICAL ENGINEERING
AT THE
MASSACHUSETTS INSTITUTE OF TECHNOLOGY

JUNE 2005

Copyright ©2005 Eli J. Weinberg. All rights reserved.



The author hereby grants to MIT permission to reproduce and to distribute publicly paper
and electronic copies of this thesis document in whole or in part.

Signature of Author _____
Department of Mechanical Engineering
May 26, 2005

Certified by _____
Dr. Mohammad R. Kaazempur-Mofrad
Assistant Professor, Department of Bioengineering, University of California Berkeley
Visiting Assistant Professor, Department of Mechanical Engineering
Thesis Supervisor

Certified by _____
Dr. Jeffery Borenstein
Charles Stark Draper Laboratory
Thesis Supervisor

Certified by _____
Dr. Lallit Anand
Professor, Department of Mechanical Engineering
Chairman, Department Committee on Graduate Students

BARKER

Dynamic Simulation of Heart Mitral Valve with Transversely Isotropic Material Model

by

Eli Weinberg

Submitted to the Department of Mechanical Engineering on May 26, 2005 in Partial Fulfillment of the requirements for the degree of Master of Science in Mechanical Engineering

ABSTRACT

This thesis develops two methods for simulating, in the finite element setting, the material behavior of heart mitral valve leaflet tissue. First, a mixed pressure-displacement formulation is used to implement the constitutive material behavior with general 3D elements. Second, a shell is formulated that incorporates the 3D material behavior by use of a local plane stress iteration method.

Both of these works are based on an existing invariant-based strain energy function that has been experimentally determined for the mitral valve leaflet tissue. Since this material is considered to be nearly incompressible, a mixed pressure-displacement (u/p) formulation is needed to apply the material model in 3D elements. The standard (u/p) formulation is employed with a modification to ensure positive definiteness of the constitutive tensor at low strains.

The shell formulation is introduced as a computationally less expensive alternative to the use of 3D elements. A 4-node shell with mixed interpolation of transverse shears is implemented. To incorporate the 3D material model into this shell, a local plane stress iteration is used to enforce that the shell stress assumption at each integration point.

Comparisons of numerical results to analytical predictions verify the accuracy of both the (u/p) formulation and shell element. These methods provide useful bases for finite element simulations of mitral heart valve behavior.

Technical Supervisor: Dr. Jeffery Borenstein
Title: Distinguished Member of the Technical Staff

Thesis Advisor: Mohammad R. Kaazempur-Mofrad
Title: Assistant Professor, Department of Bioengineering, University of California Berkeley

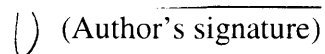
(this page left intentionally blank)

ACKNOWLEDGEMENT

May 26, 2005

Part of this project was supported by Draper Internal R&D - project number 13124.

Publication of this thesis does not constitute approval by Draper or the sponsoring agency of the findings or conclusions contained herein. It is published for the exchange and stimulation of ideas.

 (Author's signature)

(this page left intentionally blank)

Table of Contents

	page
List of Figures	9
List of Tables	11
1. Overview of Heart Mitral Valve and Project Goals	13
1.1. Heart Mitral Valve Function	14
1.2. Current Methods for Mitral Valve Replacement	15
1.3. Tissue Engineering of Heart Valves	16
1.4. Numerical Simulation of Mitral Heart Valve	17
1.5. Overall Project Goals	19
1.6. Specific Goals of This Thesis	20
2. On the Constitutive Models for Heart Valve Leaflet Mechanics	23
2.1. Introduction	23
2.2. Basic Properties of Heart Valve Tissue	23
2.3. Constitutive Models	25
2.3.1. Phenomological Models	26
2.3.2. Transversely Isotropic Models	28
2.3.3. Planar Fiber Models	29
2.3.4. Unit-Cell Models	31
2.4. Discussion	33
2.5. Conclusions	34
3. A Mixed (u/p) Formulation for Mitral Valve Leaflet Tissue Mechanics	35
3.1. Introduction	35
3.2. Continuum Mechanics Definitions	36
3.3. Experimentally Determined Strain-Energy Function for Mitral Valve Leaflet Tissue	37
3.4. Mixed (u/p) Formulation	38
3.5. Modification to Strain Energy Function	40

3.6. Software Implementation and Verification	40
3.7. Discussion	43
3.8. Conclusions	44
4. A Finite Shell Element for Heart Mitral Valve Leaflet Mechanics, with Large Deformations and 3D Constitutive Material Model	45
4.1. Introduction	45
4.2. Methods	46
4.2.1. Continuum Mechanics Definitions	46
4.2.2. Constitutive Material Model	47
4.2.3. Shell Element Description	47
4.2.4. Calculation of Stresses and Constitutive Tensor	50
4.3. Numerical Tests and Results	52
4.4. Conclusions	57
5. Conclusions and Future Directions	59
References	63
Appendix A: Derivation of All Terms for Mixed Pressure-Displacement Formulation	71

List of Figures

	page
Figure 1.1. Heart cross-section and mitral valve with labeled features	13
Figure 1.2. Example mechanical heart valve prostheses, the St. Jude Medical bileaflet tilting-disk valve	14
Figure 1.3. Carpentier-Edwards porcine aortic prosthesis	15
Figure 1.4. 3-dimensional digitized mitral valve geometry	18
Figure 1.5. Schematic of hybrid tissue engineered/synthetic mitral valve leaflet	19
Figure 1.6. Chamber and actuator of device to apply cyclic strain to thin biological and hybrid biological/synthetic membranes in an incubator	20
Figure 2.1. SEM of tricuspid valve leaflet material, showing characteristic aligned waviness	23
Figure 2.2. Uniaxial stress-strain data for fresh human mitral leaflet tissue, showing highly nonlinear and anisotropic response	24
Figure 2.3. Eight chain unit-cell model	32
Figure 3.1. Equibiaxial strain applied to anterior leaflet	41
Figure 3.2. 2:1 Off-baxial strain applied to anterior leaflet	42
Figure 3.3. Equibiaxial strain applied to posterior leaflet.	42
Figure 3.4. 2:1 Off-baxial strain applied to posterior leaflet	43
Figure 4.1. Numerical and analytical solutions for uniaxial stretching.	53
Figure 4.2. Numerical and analytical results for equibiaxial stretching of anterior leaflet	54
Figure 4.3. Numerical and analytical results for equibiaxial stretching of posterior leaflet	54
Figure 4.4. Moment versus applied rotation at tip of cantilevered element, for anterior and posterior leaflet materials with bending parallel and perpendicular to fiber direction.	55

Figure 4.5. Initial and final geometry in dynamic snapping test.	56
Figure 4.6. Applied pressure and resulting displacement versus time for dynamic snapping test	57
Figure 5.1. Normal mitral valve flattened, characteristic dimensions of explanted mitral valve leaflets, and CAD representation of mitral valve leaflet geometry	59
Figure 5.2. Mitral valve geometry meshed with three-dimensional elements	61

List of Tables

	page
Table 3.1: Coefficient Values for Mitral Valve Tissue	38

1. Overview of Heart Mitral Valve and Project Goals

1.1 Heart Mitral Valve Function

The heart mitral valve is a one-way valve allowing blood to flow from the heart's left atrium to the left ventricle. The mitral valve consists of two leaflets (also referred to as "cusps"), the anterior and the posterior, that are anchored to the papillary muscles, which are connected to the interior wall of the ventricle. The chordae tendinae are chord-like structures that connect the leaflets to the papillary muscles. This arrangement is depicted in Figure 1.1.

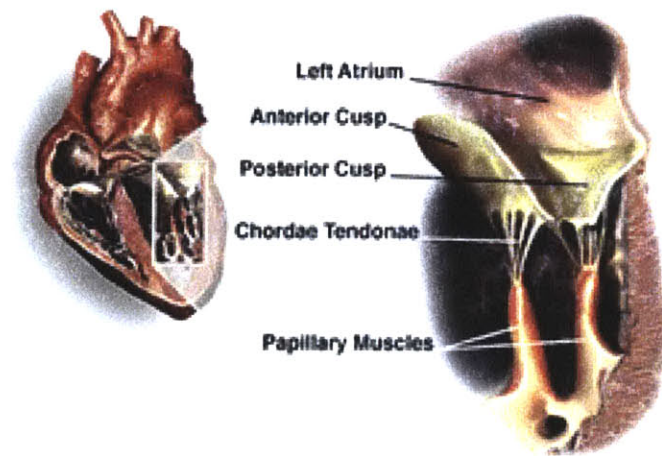


Figure 1.1. Heart cross-section and mitral valve with labeled features (Gahmbir, 2005)

When the pressure in the atrium is higher than that in the ventricle, the leaflets flap open and blood can flow through unobstructed. When the pressure is higher in the ventricle than the atrium the leaflets fold shut against each other, supported by the chordae structure, and do not allow blood to flow through.

A correctly functioning mitral valve is vital to overall heart function: if the valve either obstructs flow from the atrium to ventricle or allows flow in the opposite direction, the heart's efficiency drops radically and the heart must work harder to deliver the required flow of blood to the body. The case of a valve obstructing normal flow is known

generally as stenosis, while a valve allowing backwards flow is known as regurgitation. Both mitral stenosis and mitral regurgitation are generally caused either by congenital heart defects or by acute rheumatic fever, which can inflame, thicken, or stiffen the leaflets and damage the chordae (Roberts, 1983).

In some cases, valves that have become highly stenotic or regurgitant can be surgically repaired: examples include shortening the chordae or replacing them with artificial material (Reimink, 1996), and implanting an annuloplasty ring around the valve to support the surrounding tissue or alter the diameter of the valve (Kunzelman, 1998). Often the valve cannot be repaired, and the entire mitral apparatus must be replaced.

1.2. Current Methods for Mitral Valve Replacement

Currently, there are four types of heart valve replacements available: mechanical prosthesis, xenograft, allograft, and autograft. Here we briefly describe each and discuss their relative benefits.

Mechanical prostheses are completely composed of synthetic materials. The two common types are the caged-ball or tilted disk designs. Approximately one-half of all current valve replacements use the St. Jude Medical bileaflet tilted-disk model (Schoen and Levy, 1991), an example of which is shown in Figure 1.2. Mechanical replacements in general are more common than the other types of valve replacement. Mechanical prosthetic valves are constructed from high-strength, high-thromboresistance materials and are designed to provide minimal obstruction to blood flow.

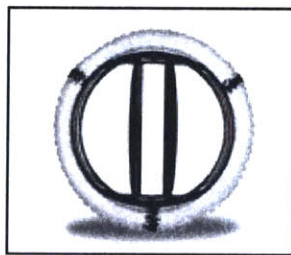


Figure 1.2. Example mechanical heart valve prostheses, the St. Jude Medical bileaflet tilting-disk valve (St. Jude Medical, 2005)

Xenograft, allograft, and autograft valves are not completely synthetic; all include at least some human or animal tissue. The term xenograft refers to tissue transplanted between species. In the context of heart valve replacement, xenografts are composed of gluteraldehyde-fixed tissue, either porcine aortic or bovine pericardium, mounted on a stent. Because of their use of biologic tissue and mechanical supports, xenograft valves are commonly referred to as bioprosthetic valves. Bioprostheses based on porcine aortic tissue represent one-third of all valve replacements. One such valve is shown in Figure 1.3. Allografts are transplants between members of the same species. An allograft heart valve is a complete valve taken from a human donor. Autografts consist of tissue taken from one part of the patient's body and implanted in another site. Tissue may be taken from a patient's pericardium or fascia lata and formed into a heart valve to create an autograft. In some cases, one of the patient's own valves can be moved to another valve location (Schoen and Levy, 1991).



Figure 1.3. Carpentier-Edwards porcine aortic prosthesis (Edwards Lifesciences, 2005)

Each type of valve replacement has advantages and disadvantages over the others. Mechanical prostheses rarely wear out, but are significantly thrombogenic and thus require lifelong anti-coagulation (blood-thinning) of the patient. Additionally, all mechanical valves cause more obstruction of blood flow than natural valves, and mechanical valves are susceptible to infection that can only be remedied by re-operation.

Tissue-based valves have better hemodynamic properties than mechanical valves and do not require anti-coagulation treatment. However, they have different associated problems. Bioprosthetic valves generally have a shorter implant life than the mechanical valves. After a few years of implantation, significant calcification (Vyavahare, 1997) and

mechanical fatigue of both the natural and synthetic components (Butany, 1990) are seen. Allografts also have durability problems (Niwaya, 1999) and, since they require a genetically matched donor, suffer from undersupply (Stark, 1998). Autografts have shown unacceptable failure rates due to shrinkage, tearing, and other effects (Silver, 1975) and are not widely used.

The development of heart valve replacement procedures over the past three decades represents an enormous medical and technological accomplishment. Each year, 40,000 heart valve replacements are performed in the US and 170,000 worldwide (Schoen, 1999), effectively curing end-stage valvular disease in many of the patients. This cure is imperfect, however. In practice, the surgeon commonly must choose between a mechanical valve, with its associated risk of thromboembolic complications, and a bioprosthetic valve with limited durability. Within 10 years of implant, approximately 50% of patients have valve-related complications (Bloomfield, 1991), and approximately 20% of all valve surgery is accounted for by re-operations on replaced valves (Schoen, 1991). Additionally, none of the approaches described above allow for remodeling of the valve, and thus cannot be used in a pediatric case where the patient is going to grow (Fuchs, 2001). In the next section, we discuss the possible advantages of a tissue-engineered heart valve over current replacement options.

1.3. Tissue Engineering of Heart Valves

Driven by the limitations of existing valve replacement options listed above, many researchers are now investigating methods to construct a replacement valve by tissue engineering. In this approach, appropriate live cells are extracted from the patient and used to fabricate a replacement valve. This method would create functioning, living valves replacements. Since natural valves have far superior thrombogenic properties, durability, and remodeling capabilities to current artificial and bioartificial valves, it is hoped that tissue engineering can create an improved valve replacement.

A heart valve leaflet is composed mainly of extracellular matrix (ECM), deposited and maintained by fibroblasts and smooth muscle cells scattered throughout the ECM. The

leaflet also has a non-thrombogenic coating of endothelial cells. The most common approach to tissue-engineer this structure is to seed fibroblasts within a degradable polymer and endothelial cells on the surface. Upon implantation, the material should dissolve in a controlled fashion to leave a completely biologic structure of ECM supported by and coated by the correct cells. Hopeful early results have been demonstrated for this approach (Sodian, 2000b; Shinoka 1996) in animal models.

In the effort to tissue engineer a heart valve, a great amount of research has taken place to create the cell manipulation techniques necessary (Perry, 2003; Laube, 2001), to seed a valve (Hoerstrup, 2002), and to find materials with the desired biocompatibility and degradation rates (Sodian, 2000a). Though the functionality of the valve is driven by the valve's mechanical properties, the study of the valve mechanics has been largely neglected in current efforts. It is well known that the nonlinear, anisotropic leaflet tissue behavior is vital to valvular function, but studies in tissue engineered heart valves have considered the material to be linear elastic and isotropic (Booth, 2002), if they consider the material properties at all. Current efforts in the tissue engineering of heart valves can be greatly enhanced by analysis of the mechanical behavior of the heart valve structure.

1.4. Numerical Simulation of Mitral Heart Valve

Finite element analysis is a powerful tool for investigating the mechanical behavior of the mitral valve. A number of numerical models of the mitral valve have been published. Such a model of generally consists of three components: a description of the physical geometry, a constitutive model for the solid mechanics, and a description of the fluid behavior.

Mitral valve geometry has been painstakingly measured by various researchers. Measurements have been taken from thousands of excised valves, (Rusted, 1952) and the full 3-D geometry has been determined by digitizing cross-sections of the apparatus (Kunzelman, 1994).

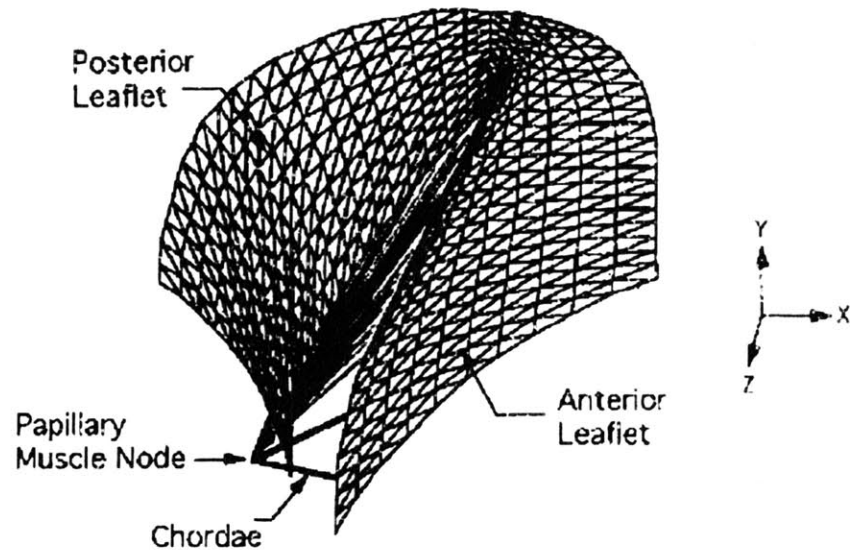


Figure 1.4. 3-dimensional digitized mitral valve geometry (Kunzelman, 1994)

Other researchers have contributed histological measurements and echocardiograph images to provide a full description of the valve's geometry.

Early finite element models of the mitral valve described the fluid behavior simply as pressure boundary conditions applied to the leaflet surfaces and an inertial component (Kunzelman, 1993). Recent models perform fluid-structure interaction to determine the complete dynamic solid and fluid behavior of the system (Einstein, 2004).

The leaflet material exhibits highly non-linear, anisotropic stress-strain behavior. Currently, no valve simulations have been published where the full three-dimensional material behavior is included. Shell models have captured the three-dimensional stress state but without an accurate material model (Kunzelman, 1993; Votta, 2002.), and membrane models have rigorously handled the in-plane deformations without bending or out-of-plane shear stresses (Einstein, 2004). A description of the 3D stress-deformation behavior of the tissue is known (May-Newman and Yin, 1998), and numerical tools are available for implementing such a description in the finite element setting. Thus, a numerical simulation of the mitral valve including accurate 3D material constitutive behavior is possible.

1.5. Overall Project Goals

The computational methods discussed in this thesis are part of a larger project, in collaboration with Massachusetts General Hospital's Department of Cardiovascular Surgery, to create a mitral valve replacement combining synthetic and tissue engineered components. A hybrid valve could have the non-thrombogenic and remodeling capabilities of a fully tissue-engineered valve, but a skeleton of synthetic material would provide support for the cells and ECM. The support structure would ease manipulation of the valve before the cells and ECM fully mature, and would make possible attachment of the thin chordae tendinae to the rest of the structure. A schematic of the design is shown in Figure 1.5. The synthetic components will likely consist of segmented polyurethane, which is highly elastic, has been used in other cardiovascular applications, has low thrombogenicity, and has excellent durability (Hayashi, 1994), and ePTFE, the flexible but nearly inextensible material currently used for sutures in valve surgery.

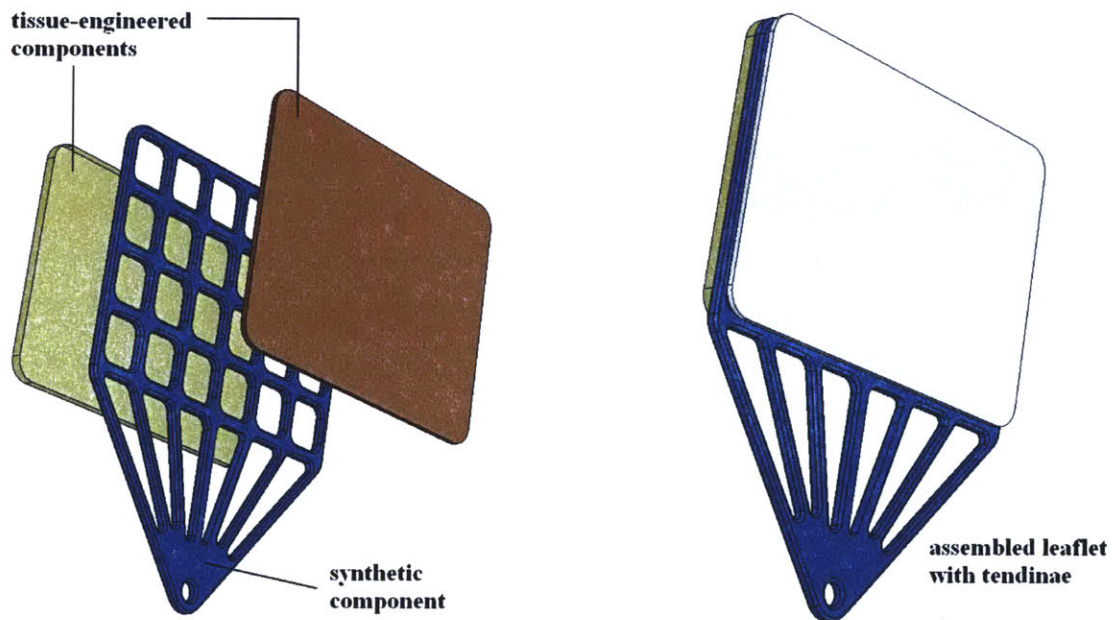


Figure 1.5. Schematic of hybrid tissue engineered/synthetic mitral valve leaflet

The design of such a structure requires an understanding of how each mechanical component affects the overall function and the ability to control the mechanical parameters. Towards controlling the mechanical parameters, we have developed a set of

physical tools for the production and measurement of biological and hybrid tissues of the size scale needed for mitral application. Figure 1.6. shows a device we designed to apply cyclic strain to a thin tissue for long periods of time in an incubator environment, a necessary condition for creation of proper ECM.

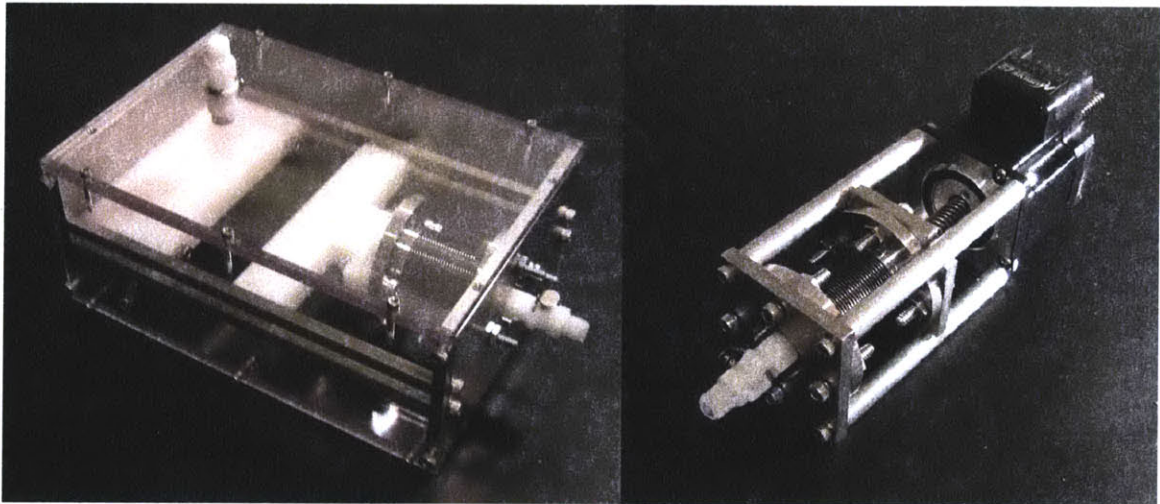


Figure 1.6. Chamber (left) and actuator (right) of device to apply cyclic strain to thin biological and hybrid biological/synthetic membranes in an incubator.

In order to achieve our ultimate goal of design and manufacture of the hybrid synthetic/tissue engineered mitral valve, a computational model of the heart valve motion that includes the material effects is crucial as the model allows us to evaluate prospective hybrid designs through simulation. Such a model could also be used to investigate the mechanics of normal and abnormal mitral valve function. In this thesis, we develop numerical tools necessary for this purpose.

1.6. Specific Goals of This Thesis

The goal of this thesis is to develop methods for simulating mitral valve material in the finite element setting. To be useful in simulating the motion of mitral valve leaflets, these material models must be robust, accurate, and computationally efficient. We begin in Chapter 2 by reviewing relevant analytical models for the stress-deformation behavior of thin biological materials. From these, we select one particular model that is accurate in modeling mitral valve leaflet mechanics, general to three-dimensional deformations, and appropriate for numerical implementation. In Chapter 3, the analytical material model is

implemented in general three-dimensional elements by application of a mixed pressure-displacement formulation. We show this model to be accurate by comparison to analytical and experimental data. This implementation is useful for simulating leaflet mechanical behavior, but its requirement of high-order three-dimensional elements is computationally expensive for simulating the whole valve. In Chapter 4, we develop and implement a computationally inexpensive method. By using a local plane-stress algorithm, the analytical material model is incorporated into a 4-node MITC shell element. The shell includes all three-dimensional deformation effects, and thus is as effective as the mixed formulation while representing a significant computational savings. In Chapter 5, we discuss the future uses for the numerical tools we have introduced.

2. On the Constitutive Models for Heart Valve Leaflet Mechanics

2.1 Introduction

Any numerical implementation of a material behavior must be based on an accurate description of the material. Numerous constitutive models have been developed to describe heart valve tissue and other similar biological tissues. In this chapter we discuss the observed behavior of heart valve leaflet tissue and review analytical models proposed to describe the mechanical behavior.

2.2. Basic Properties of Heart Valve Tissue

The basic physical properties of heart valve tissue govern the assumptions that can be made in the formulation of a constitutive model. Heart valve tissue consists of a fibrous tissue network, mainly collagen and elastin, saturated with a fluid that is mostly water. SEM of leaflet tissue shows that the fibrous network is wavy and uniaxially aligned (see Figure 2.1).

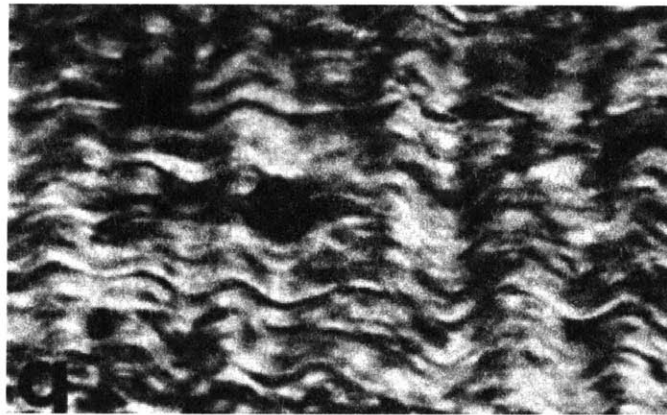


Figure 2.1. SEM of tricuspid valve leaflet material, showing characteristic aligned waviness (Broom,1978).

The aligned fibers of the leaflet tissue make the stress-strain response highly anisotropic. Tensile testing (Billiar and Sacks, 2000a) has shown that the aortic leaflets are significantly stiffer in the circumferential direction than the radial direction, and similar results have been recorded for mitral valve tissue (Clark, 1973). Data for mitral valve

tensile testing is shown in Figure 2.2.

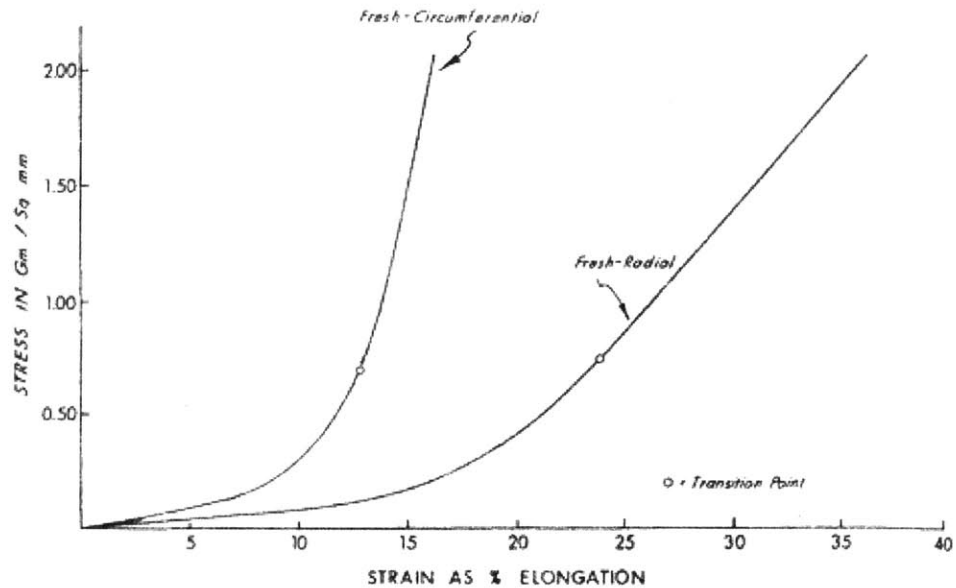


Figure 2.2. Uniaxial stress-strain data for fresh human mitral leaflet tissue, showing highly nonlinear and anisotropic response (Clark, 1973).

A material supported by uniaxially aligned fibers can be described by a special case of anisotropy known as transverse isotropy. In transverse isotropy, the material has one preferred direction parallel to the fiber direction, and the responses in every direction perpendicular to the preferred direction are identical to each other.

The waviness of the fibers also significantly affects the stress-strain response. Generally, less force is required to stretch a wavy fiber than a straight fiber. At low strains, the fibers in heart valve tissue are wavy, and the tissue can be extended by relatively low stresses. As strains increase, the fibers are straightened, and the stress required to extend the tissue increases dramatically. This nonlinear response is evidenced in Figure 2.2, as the slope of the stress-strain curve increases with increasing strain.

Water comprises between 60% and 70% of a collagenous tissue by weight (Weiss, 1996). This volume of water appears to be tightly bound to the fibrous network, as evidenced by fact that it is difficult to exude any significant amount of fluid by compression (Hvidberg, 1960). Thus, models should consider the tissue to be nearly or completely incompressible

(Weiss, 1996; Holzapfel, 1995; May-Newman and Yin, 1998).

Since the tissue consists of a combination of solid and fluid components, it would be natural to assume that the solid component would contribute an elastic response to loading and the fluid component would contribute a viscous response, so that the overall response would be viscoelastic. It has been shown, however, that biological tissues can be preconditioned by repeatedly loading and unloading the specimen (Fung 1967, Fung 1993). After a number of cycles, the response will reach a steady state where the tissue shows one non-linear response for the loading phase and a separate non-linear response for the unloading cycle. Once this steady state has been reached, both phases are insensitive to the loading rate: the viscous effect disappears after preloading. A material with this response can be treated as one hyperelastic material in loading, and a separate material in unloading. Such behavior, known as pseudoelasticity, has been shown to apply to heart valve tissue (May-Newman and Yin, 1995).

A constitutive model for heart valve tissue must incorporate all of the features listed above: it should describe a pseudoelastic, incompressible, anisotropic, nonlinear material. While relatively few models have been formulated specifically for heart valve tissue, a number of models exist for biological soft tissues in general and for similar tissues.

2.3. Constitutive Models

This section surveys a few different derivations for the stress-strain behavior of heart valve and similar tissues. These derivations include a range of information about the structure of the tissue, from phenomenological models that include no information about the structure to unit-cell models that are derived completely from the observed fibrous structure.

Many constitutive models for biological tissues are derived by extending theories developed for rubber deformation. Rubber models apply generally to large-strain, isotropic, hyperelastic materials, therefore extending these models to include anisotropic, pseudoelastic behavior creates models appropriate for biological tissues. The essential

concept of this class of theory is that the energy density in the material can be determined as a function of the strain state. Once the strain-energy function W is known, the stress state can be determined by taking the derivative of W with respect to a strain measure, such as

$$\mathbf{S} = \frac{\partial W}{\partial \boldsymbol{\varepsilon}}, \quad (2.1)$$

where \mathbf{S} is the 2nd Piola-Kirchhoff stress tensor and $\boldsymbol{\varepsilon}$ is the Green-Lagrange strain tensor. One form commonly used to determine stresses for the materials considered here is

$$\boldsymbol{\sigma} = -p\mathbf{I} + \mathbf{F} \cdot \frac{\partial W}{\partial \boldsymbol{\varepsilon}} \cdot \mathbf{F}^T, \quad (2.2)$$

where $\boldsymbol{\sigma}$ is the Cauchy stress tensor, \mathbf{F} is the deformation gradient, p is a Lagrange multiplier to enforce incompressibility, and \mathbf{I} is the identity matrix (Holzapfel, 2001).

2.3.1. Phenomological Models

A phenomological model is typically developed by guessing either a form of the stress-strain response or of the strain-energy function. The resulting stress-strain response is then fit to experimental stress-strain data.

A large-strain constitutive model can be formulated by extension of one of the many well-known models for linear elastic materials. Li, have created a model for heart valve tissue by extending the linear transversely isotropic model (Li, 2001). The stress-strain relation for the linear transversely isotropic model is

$$\boldsymbol{\sigma} = [\mathbf{E}]\boldsymbol{\varepsilon}, \quad (2.3)$$

where the stiffness matrix $[\mathbf{E}]$ is a function of one Young's modulus in the direction parallel to the main fiber E_x and one perpendicular E_y , two Poisson's ratios ν_{xy} and ν_{yx} , and a shear modulus G_{xy} . Here the nonlinear material behavior is accounted for by letting the Young's moduli with an effective strain $\bar{\varepsilon}$,

$$\bar{\varepsilon} = \frac{\sqrt{(\varepsilon_x - \varepsilon_y)^2 + (\varepsilon_z - \varepsilon_y)^2 + (\varepsilon_x - \varepsilon_z)^2 + \frac{3}{2}(\gamma_{xy}^2 + \gamma_{yz}^2 + \gamma_{xz}^2)}}{\sqrt{2}(1 + \nu)}. \quad (2.4)$$

E_x and E_y are assumed to have exponential forms, and fitting to uniaxial strain data gives:

$$\begin{aligned} E_x &= 1927.2e^{9.827\epsilon_x}, \\ E_y &= 118.34e^{13.20\bar{\epsilon}}. \end{aligned} \quad (2.5)$$

with $E_x \gg E_y$, G_{xy} can be calculated in the linear elastic sense from

$$G_{xy} = \frac{E_y}{2(1 + \nu_{xy})}, \quad (2.6)$$

and the two Poisson's ratios are assumed to be equal 0.45 at all strains to represent incompressible tissue. This model is reported to achieve a good fit with uniaxial data from porcine aortic heart valve.

Many models exist that are based on an assumed strain-energy function for the tissue. Based on observations for rat mesentery, Fung and co-workers (Tong and Fung, 1974) proposed that that the strain energy should be exponentially related to the strain,

$$W = \frac{c}{2}(e^Q - 1), \quad (2.7)$$

where c is a constant and Q is a function of the strain state such as

$$Q = c_{ijk} \epsilon_{ij} \epsilon_{kl}, \quad (2.8)$$

where all c 's are material constants and ϵ_{ij} is the i - j term of the Green-Lagrange strain.

A similar function can be written including only planar tension terms

$$W = B_0 \left[\exp\left(\frac{b_1 E_{11}^2}{2}\right) + \exp\left(\frac{b_2 E_{22}^2}{2}\right) + \exp\left(\frac{b_3 E_{11} E_{22}}{2}\right) - 3 \right], \quad (2.9)$$

where B_0 , b_1 , b_2 , and b_3 are constants. This function fits well with canine pericardium biaxial data (Choi and Vito, 1990). When the coupling terms is removed to leave

$$W = \frac{c}{2} \left[\exp(A_1 \epsilon_{11}^2 + A_2 \epsilon_{22}^2) - 1 \right], \quad (2.10)$$

where A_1 and A_2 are constants, only a poor fit could be achieved with biaxial human aortic tissue data (Billiar and Sacks, 2000b).

2.3.2. Transversely Isotropic Models

The models in this section determine strain-energy functions based on the assumption of transverse isotropy and in terms of strain invariants. Transverse hyperelasticity can be completely described by the three strain invariants and two pseudo-invariants (Holzapfel, 2001). The three basic invariants are

$$I_1 = \text{tr}(\mathbf{C}), I_2 = \frac{1}{2} \left[(\text{tr} \mathbf{C})^2 - \text{tr}(\mathbf{C}^2) \right], I_3 = \det(\mathbf{C}), \quad (2.11)$$

where \mathbf{C} is the right Cauchy-Green deformation tensor and the two pseudo-invariants are

$$I_4 = \mathbf{N} \cdot \mathbf{C} \cdot \mathbf{N}, I_5 = \mathbf{N} \cdot \mathbf{C}^2 \cdot \mathbf{N}, \quad (2.12)$$

where \mathbf{N} is a vector describing the local fiber direction.

Stress-strain data suggests that the strain-energy function of passive myocardium depends strongly on I_1 and I_4 , and is independent of the other invariants (Humphrey and Yin, 1989). Thus, a subclass of transversely isotropic materials is defined by I_1 and α , where α is the stretch in the fiber direction,

$$\alpha^2 = I_4. \quad (2.13)$$

The strain strain-energy function may be broken into two independent isotropic and anisotropic contributions,

$$W = W_I + W_A, \quad (2.14)$$

where each term is represented by a Fung-like exponential,

$$W = W_I + W_A = c \left\{ \exp[b(I_1 - 3)] - 1 \right\} + A \left[\exp[a(\alpha - 1)^2] - 1 \right]. \quad (2.15)$$

This function mimics the biaxial myocardium data reasonably well (Humphrey and Yin, 1989).

Other functions of I_1 and α have been proposed, such as

$$W = c_1(\alpha - 1)^2 + c_2(\alpha - 1)^3 + c_3(I_1 - 3) + c_4(I_1 - 3)(\alpha - 1) + c_5(I_1 - 3)^2. \quad (2.16)$$

This function was formulated to fit one specific set of data, and achieved fairly accurate predictions of biaxial data that was not included in the formulation (Humphrey, 1990).

A transversely isotropic strain-energy function can be written with analogy to the exponential form of Equation 2.7,

$$Q = c_1(I_1 - 3)^3 + c_2(\alpha - 1)^4. \quad (2.17)$$

This equation achieved favorably agreed with biaxial data from both mitral valve leaflets (May-Newman and Yin, 1998). It should be noted that this formulation requires only three coefficients, c_1 and c_2 from Equation 2.20 and c from Equation 2.7.

2.3.3. Planar Fiber Models

The models in this section take a variety of approaches to tie the overall tissue behavior to the behavior of a single fiber or bundle of fibers. A strain-energy function or stress function may be proposed for a single fiber or group of fibers, then geometric assumptions are used to extrapolate the stress-strain or strain-energy model for the whole tissue.

Again the strain-energy function can be broken into components. In this case (Humphrey and Yin, 1987), it is assumed that the fluid matrix, collagen, and elastin each contribute independent terms to the strain-energy,

$$W = W_m + \sum W^c + \sum W^e, \quad (2.18)$$

where W_m is the strain-energy function of the fluid matrix, and W^c and W^e are the collagen and elastin components, respectively. The fiber components must be summed to represent fibers oriented in different directions. Elastin behaves generally as a linear spring, so its behavior is represented by

$$W^e = b[\gamma - \ln \gamma - 1], \quad (2.19)$$

where b is a constant and γ is the stretch ratio in the direction of the elastin fiber, and represents the net effect of the collagen fibers by

$$W^c = A\{\exp[a(\beta - 1)^2] - 1\}, \quad (2.20)$$

where A and a are constants and β is the stretch ratio in the direction of the collagen fiber. The summation of the fiber strain energy terms for a transversely isotropic material is evaluated as

$$W = \sum W^c + \sum W^e = \int_0^\pi (W^c + W^e) d\phi, \quad (2.21)$$

where ϕ represents an angle in the plane of the tissue. The fluid matrix is assumed to contribute only a hydrostatic pressure, which is incorporated into the Lagrange multiplier in Equation 2.2. This function was shown to fit pleura data reasonably well (Humphrey and Yin, 1987).

Separate models have been proposed for collagen and elastin fibers (Lanir, 1979). The force to extend an elastin fiber is

$$F_e = K_e [\lambda - 1], \quad (2.22)$$

where K_e is the spring constant for an elastin fiber and λ is the stretch ratio of the fiber. A crimped collagen fiber is assumed to stretch with zero force until it is straightened, and once it is straightened acts as a linear spring,

$$F_c \begin{cases} 0, & \lambda < \lambda_c \\ K_c [\lambda - \lambda_c], & \lambda > \lambda_c \end{cases}, \quad (2.23)$$

where λ_c is the critical stretch needed to straighten the fiber and K_c is the spring constant for a straightened collagen fiber. This work also proposed that, rather than calculating exactly when each collagen fiber reaches its straightening stretch, a probability function can be used to determine what percentage of fibers are straight for any tissue strain state (Lanir, 1979). Subsequent models generally ignore the elastin component to model the network entirely in terms of probabilistic collagen fibers (Lanir, 1982).

One such model based on the previous work represents the fiber stress-strain relationship with

$$\sigma_f(\varepsilon_f) = K_2 \int_0^{\varepsilon_f} D(x) \frac{\varepsilon_f - x}{1 + 2x} dx, \quad (2.24)$$

where σ_f and ε_f are the stress and strain in the fiber, respectively, x is the variable of integration, and $D(x)$ is defined by a Gamma distribution,

$$D(x) = \frac{1}{\beta^\alpha \Gamma(\alpha)} x^{\alpha-1} \exp\left(-\frac{x}{\beta}\right), \quad (2.25)$$

where α and β are positive constants. The tissue stress-strain relationship can then be

found by

$$\boldsymbol{\sigma} = \int_{-\pi/2}^{\pi/2} R(\theta) \boldsymbol{\sigma}_f(\boldsymbol{\varepsilon}_f) [N \otimes N] d\theta, \quad (2.26)$$

where R represents the angular distribution of the fibers. The fiber stress-strain relation can also be represented by

$$\boldsymbol{\sigma}_f(\boldsymbol{\varepsilon}_f) = A[\exp(B\boldsymbol{\varepsilon}_f) - 1], \quad (2.27)$$

where A and B are constants, and both Equation 2.27 and Equation 2.30 have good fit and predictive ability for bovine pericardium biaxial data (Sacks, 2003). Equation 2.30 has been found to give a good fit and predictive behavior for biaxial aortic valve cusp samples (Billiar and Sacks, 2000b).

2.3.4. Unit-Cell Models

A common approach in the constitutive modeling of rubber and elastomer materials is to derive the entire model from knowledge of the material's microstructure. Entropy-based models are used to predict the behavior of a single fiber and a unit-cell approach is used to determine the bulk tissue properties. Many such models have been presented for modeling of rubber; for a review the reader is directed to Boyce and Arruda, 2000. Rubber models are generally isotropic, so modeling of heart valve tissue and the like requires extension to anisotropy. Unit cell models can be readily extended to orthotropy, and the derivation of one such model is followed here.

The strain-energy equation for a single fiber can be determined using a freely-jointed or wormlike chain model. Using a Langevin freely-jointed chain model appropriate for large strains gives the increase in strain energy from undeformed length R to deformed length r for a chain of total length L ,

$$\Delta w = k_B \Theta N \left[\left(\frac{\rho}{N} \beta_\rho + \ln \frac{\beta_\rho}{\sinh \beta_\rho} \right) - \left(\frac{P}{N} \beta_P + \ln \frac{\beta_P}{\sinh \beta_P} \right) \right], \quad (2.28)$$

where k_B is Boltzmann's constant, Θ is the absolute temperature, N is the number of links in a single chain, and ρ and P are the normalized chain lengths r/L and R/L , respectively (Bischoff, 2002). β is defined by the inverse Langevin function so that $\beta_\rho = \mathcal{L}^{-1}(\rho)$

$\lambda(\rho/L)$, $\beta_R = L^{-1}(R/L)$. Using an eight chain unit-cell model, as shown in Figure 2.3, the strain energy needed to stretch the chains within the cell is

$$w_{chains} = w_0 + 2k_B \Theta N \sum_{i=1}^4 \left[\frac{\rho^{(i)}}{N} \beta_\rho^{(i)} + \ln \frac{\beta_\rho^{(i)}}{\sinh \beta_\rho^{(i)}} \right], \quad (2.29)$$

where i sums over half of the chains.

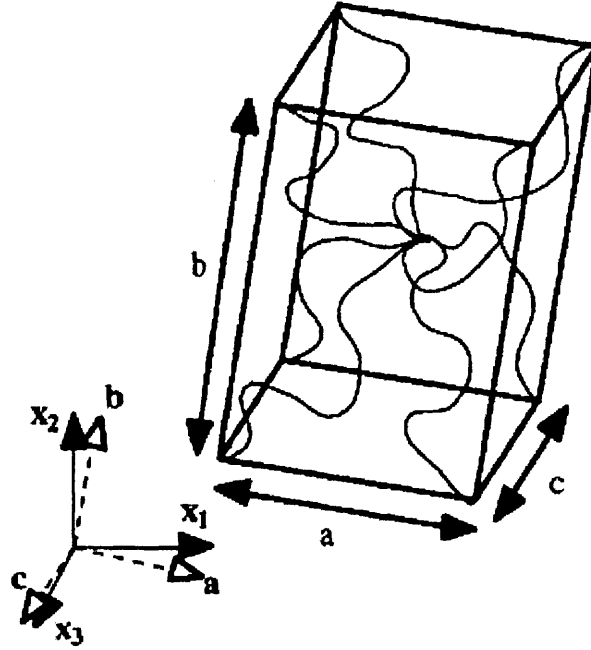


Figure 2.3. Eight chain unit-cell model (Bischoff, 2002).

There also exists a strain energy due to repulsion between the chains,

$$w_{repulsion} = \frac{8k_B \Theta \sqrt{N} \beta_p}{a^2 + b^2 + c^2} \ln(\lambda_a \lambda_b \lambda_c), \quad (2.30)$$

where a , b , and c are the dimensions shown in Figure 2.3 and λ_a , λ_b , and λ_c are the stretches in the directions along the principal material axes. Assuming the material is incompressible, the complete strain energy function is given by

$$W = \sum_{n/8} \frac{n}{8} (w_{chain} + w_{repulsion}), \quad (2.31)$$

where n is the chain density. N can be directly related to a , b , and c , so this model is applicable with four free variables: n , a , b , and c . This function provides a good fit to uniaxial skin data (Bischoff, 2002).

2.4. Discussion

The main challenge in constructing a constitutive model for heart valve leaflet tissue is that the tissues are thin, and experimentally can only be rigorously tested in states of planar tension. In normal heart valve function, however, the leaflets are subjected to significant out-of-plane and compressive stresses. The researcher's task is to create a model from two-dimensional data that will predict three-dimensional behavior.

While heart valve tissue cannot be readily tested in three-dimensions, results from other materials show that some of the models presented here apply in three-dimensional states. Microstructural unit-cell models have been verified in three-dimensional stress states in rubber (Boyce and Arruda, 2000) and transversely isotropic models have been similarly verified in artificial (Kominar, 1995) and biological materials (DiSilvestro, 2001). The planar fiber and phenomenological models are generally formulated only for the in-plane stresses and are not applicable to three-dimensional stress situations.

The unit-cell and transversely isotropic models seem equally applicable to describing the behavior of heart valve tissue, and researchers have achieved similar results fitting either model to biaxial data. There are some differences between the two classes of models that may help in deciding which to use. Equation 2.17 has the advantage that its constants can be determined in a relatively straightforward fashion through constant-invariant tests, while finding the constants of a unit-cell model requires fitting curves to multiple sets of data. A unit-cell model includes data on the microstructure of the material, and therefore may be preferred when the microstructural features are of interest. The numerical implementation of an invariant-based approach may be computationally cheaper than that of the unit-cell model simply by virtue of a simpler strain-energy function (Equation 2.17 versus Equations 2.28-2.31).

There are effects that none of these models incorporate. Heart valve leaflets are composed of three layers known to have different mechanical properties from each other (Vesely and Noseworthy, 1992) while all of these models assume that the material is

homogenous through the thickness. A better model would either include the three different layers as one laminated body or provide three separate regions, each with a different constitutive model. All three of the layers are structurally similar, so the model for each layer can be in the same form as the homogenous models shown in this paper. Additionally, the pseudoelastic behavior observed in uniaxial testing (Fung, 1967) has not been extended to multidimensional deformations.

2.5. Conclusions

We have reviewed a number of various models proposed for heart valve leaflet or similar biological tissue. Of these, the unit-cell microstructural models and the transversely isotropic models are applicable to describing a general three-dimensional stress-strain state. An invariant-based strain-energy function (Equation 2.7 with Equation 2.17) has been rigorously determined for heart mitral valve leaflet tissue. We determine that this function is appropriate for the specific application of numerical simulation for the mitral valve.

3. A Mixed (u/p) Formulation for Mitral Valve Leaflet Tissue Mechanics

3.1. Introduction

This chapter presents a method for implementing the invariant-based constitutive model for mitral valve leaflet tissue in the finite element setting. A mixed pressure-displacement formulation is used so that the material model can be used with general 3D elements. A modification is made to the strain energy function to aid in maintaining positive definiteness of the stiffness matrix at low strains. The numerical implementation is shown to be accurate in representing the analytical model of material behavior. The mixed formulation is useful for modeling of soft biological tissues in general, and the model presented here is applicable to finite element simulation of mitral valve mechanics.

Much research has been done in determining material constitutive models for soft biological tissues. In the previous chapter we reviewed models specific to heart valve tissue. We have identified a transversely isotropic hyperelastic representation of mitral valve leaflet tissue (May-Newman and Yin, 1998) as applicable for implementation in finite elements.

We implement the model for use with general 3D finite elements by following the mixed pressure-displacement (u/p) formulation of Sussman and Bathe (1987). A number of similar finite element implementations have been published for incompressible, transversely isotropic materials (Holzapfel, 2001; Almeida and Spilker, 1998; Rüter and Stein, 2000; Schröder and Neff, 2003). We introduce a modification to the strain energy function in order to maintain positive definiteness of the stiffness matrix at low strains with the exponential form of the strain-energy function. The implemented model is verified by comparing the numerical solution to analytical results, showing that the implementation accurately represents the original strain-energy function.

3.2. Continuum Mechanics Definitions

All calculations here are performed in terms common to large-strain continuum mechanics. The deformation gradient is denoted as

$$\mathbf{F} = \frac{\partial \mathbf{x}}{\partial \mathbf{X}}, \quad (3.1)$$

where \mathbf{X} is the original (undeformed) configuration and \mathbf{x} is the deformed configuration. The right Cauchy-Green deformation tensor is

$$\mathbf{C} = \mathbf{F}^T \cdot \mathbf{F}, \quad (3.2)$$

the strain invariants in terms of \mathbf{C} are

$$\begin{aligned} I_1 &= \text{tr} \mathbf{C}, \\ I_2 &= \frac{1}{2} \left((\text{tr} \mathbf{C})^2 - \text{tr} \mathbf{C}^2 \right), \\ I_3 &= \det \mathbf{C}. \end{aligned} \quad (3.3)$$

and the Jacobian is $J = \sqrt{I_3}$. Transverse isotropy is incorporated into the model by introducing a vector that defines the preferred fiber direction of the material. Denoting the vector as \mathbf{N} , the stretch in the fiber direction is

$$\alpha = \sqrt{\mathbf{N} \cdot \mathbf{C} \cdot \mathbf{N}}, \quad (3.4)$$

and two pseudo-invariants can be defined in terms of the right Cauchy-Green strain (Spencer, 1972):

$$I_4 = \mathbf{N} \cdot \mathbf{C} \cdot \mathbf{N} = \alpha^2, \quad (3.5)$$

$$I_5 = \mathbf{N} \cdot \mathbf{C}^2 \cdot \mathbf{N}.$$

The stress state is calculated from the deformation state based on a strain energy function,

W ,

$$\mathbf{S} = 2 \frac{\partial W}{\partial \mathbf{C}} \quad (3.6)$$

where \mathbf{S} is the 2nd Piola-Kirchoff stress tensor, and the Cauchy stresses can be determined by

$$\boldsymbol{\sigma} = J^{-1} \mathbf{F} \cdot \mathbf{S} \cdot \mathbf{F}^T. \quad (3.7)$$

The material constitutive tensor is

$$\mathbf{C} = 4 \frac{\partial^2 W}{\partial \mathbf{C}^2}. \quad (3.8)$$

The three invariants described in Equation 3.3 are recognized to describe isotropic hyperelasticity. Spencer (1972) has shown that the full set of five invariants, defined in Equation 3.3 and Equation 3.5 can be used to describe the strain-energy function of transversely isotropic hyperelasticity.

3.3. Experimentally Determined Strain-Energy Function for Mitral Valve Leaflet Tissue

A strain energy function for mitral valve leaflet tissue was carefully determined and verified by May-Newman and Yin (1995, 1998). The mitral tissue's stress-deformation response was shown to be chiefly a function of the first invariant and the stretch in the fiber direction,

$$W = W(I_1, \alpha). \quad (3.9)$$

Specifically, the response was modeled by a form analogous to the exponential proposed by Fung (1967),

$$W(I_1, I_4) = c_0 \left\{ \exp \left[c_1 (I_1 - 3)^2 + c_2 (I_4^{1/2} - 1)^4 \right] - 1 \right\}, \quad (3.10)$$

where c_0 , c_1 , and c_2 are constants fit to the experimental data, and we have used Equation 3.5 to substitute I_4 for α . The anterior and posterior leaflets have slightly different responses, reflected by the difference in values for the three constants shown in Table 1.

Table 3.1: Coefficient Values for Mitral Valve Tissue

	c_0 [kPa]	c_1	c_2
Anterior	0.399	4.325	1446.5
Posterior	0.414	4.848	305.4

The strain-energy function in Equation 3.10 along with the coefficient values in Table 1 accurately predict the stress-deformation behavior of the leaflet tissue.

3.4. Mixed (u/p) Formulation

In the modeling of incompressible and nearly incompressible solid media, a displacement-based finite element formulation gives large errors in the predicted stresses. An involved discussion of these errors is provided in Bathe (1996). A formulation where the material is considered to be nearly incompressible and the nodal displacements and pressures are separately interpolated is considered to be the most attractive for modeling these materials. Sussman and Bathe (1987) refer to such an approach as a mixed displacement-pressure (u/p) formulation and provide a general framework. Here we apply the mixed formulation to the above energy function.

The deformation gradient is determined by standard method from the displacements (see Bathe, 1996 for details), from which the invariants of Equations 3.3 and 3.5 are calculated. The original strain-energy function must be made insensitive to volume changes. This is done by substituting modified invariants for the original invariants (Weiss, 1996),

$$\begin{aligned} J_1 &= I_1 I_3^{-1/3}, \\ J_4 &= I_4 I_3^{-1/3}, \end{aligned} \quad (3.11)$$

and we follow Sussman and Bathe (1987) in defining $J_3 = \sqrt{I_3}$.

Defined as such, J_1 and J_4 are dependent on deviatoric deformations and independent of volumetric changes. Substituting these modified invariants into the original strain-energy function gives a strain-energy term that is completely deviatoric and determined entirely by the displacements,

$$\bar{W}(J_1, J_4) = c_0 \left\{ \exp \left[c_1 (J_1 - 3)^2 + c_2 (J_4^{1/2} - 1)^4 \right] - 1 \right\}, \quad (3.12)$$

where the overbar denotes quantities determined as functions solely of the nodal displacements.

An additional potential is supplied by Sussman and Bathe to include the effect of the interpolated pressure,

$$Q = -\frac{1}{2} (\bar{p} - \tilde{p})^2, \quad (3.13)$$

where \tilde{p} is the interpolated pressure and \bar{p} is the pressure determined by displacements,

$$\bar{p} = -\kappa (J_3 - 1). \quad (3.14)$$

The complete strain energy function is then

$$W = \bar{W} + Q. \quad (3.15)$$

The stresses and material stiffness tensor are found by substituting Equation 3.15 into

Equations 3.6-3.8, and the steps for assembling the element matrix entries from the strain energy function are given in Bathe, 1996.

3.5. Modification to Strain Energy Function

Efficient solution of the global finite-element matrices may require a positive definite stiffness matrix, so we would like the stiffness matrix derived here to be positive definite. The stiffness associated with the exponential strain energy function approaches the zero matrix at zero strains. We add a term to Equation 3.15 to ensure that the matrix can be decomposed at low strains,

$$W^{(PD)}(J_1) = c_{PD}(J_1 - 3), \quad (3.16)$$

where c_{PD} is a constant small enough to guarantee that $W^{(PD)} \ll W$, so that $W^{(PD)}$ does not contribute appreciably to the stress response. $W^{(PD)}$ may be recognized as the first term in a standard Mooney-Rivlin model. The strain energy function is now

$$W = \bar{W} + Q + W^{(PD)}. \quad (3.17)$$

See Appendix A for a derivation of all terms required to evaluate Equations 3.7 and 3.8.

3.6. Software Implementation and Verification

The formulation derived above was implemented as a user-supplied material model in the finite element package ADINA (ADINA R & D, Inc. Watertown). To verify the constitutive model, a unit-length cube of tissue was and meshed with a single 27 node solid element. 27 node interpolation was used for displacements and 8 node interpolation for pressures. Full Gauss integration was used for all terms. The fiber direction N was aligned with the x -axis. Uniaxial and biaxial strain conditions were simulated by applying displacements to the tissue boundaries in the x - and y - directions. Material constants listed in Table 3.1 were used, along with $c_{PD}=10^{-8}$ and $\kappa=10^6$ Pa.

To verify the material model, the tissue was subjected to biaxial strain conditions replicating experiments run by May-Newman and Yin (1998). The range of stresses in these experiments is consistent with the range of stresses expected in a functioning mitral valve (Kunzelman, 1993). Resulting stresses output by the finite element solution were compared to the analytical solution (see Figures 3.2-3.5). The analytical responses were found by applying biaxial strain conditions, solving for the out-of-plane strain directly from incompressibility, and calculating the stresses from the original strain-energy function. We also include the experimental data on the plots. In all cases, the stress in the direction parallel to the fiber is plotted against the stretch in the fiber direction, and the stress in the direction perpendicular to the fiber is plotted versus the stretch perpendicular to the fiber.

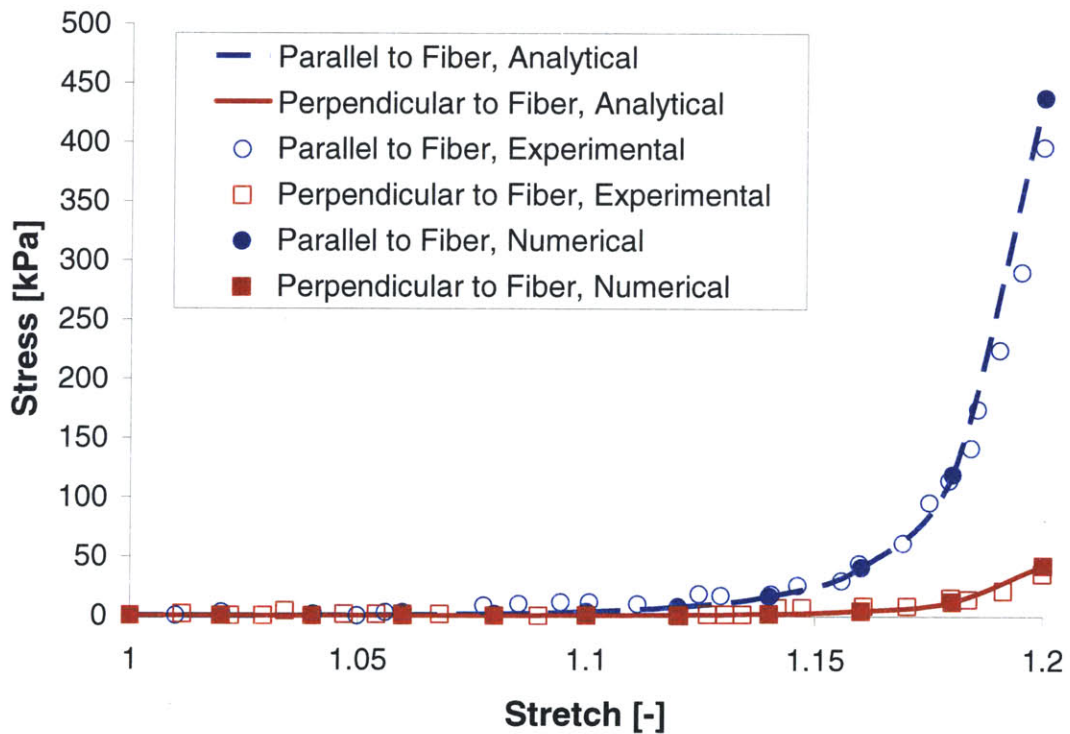


Figure 3.1. Equibiaxial strain applied to anterior leaflet.

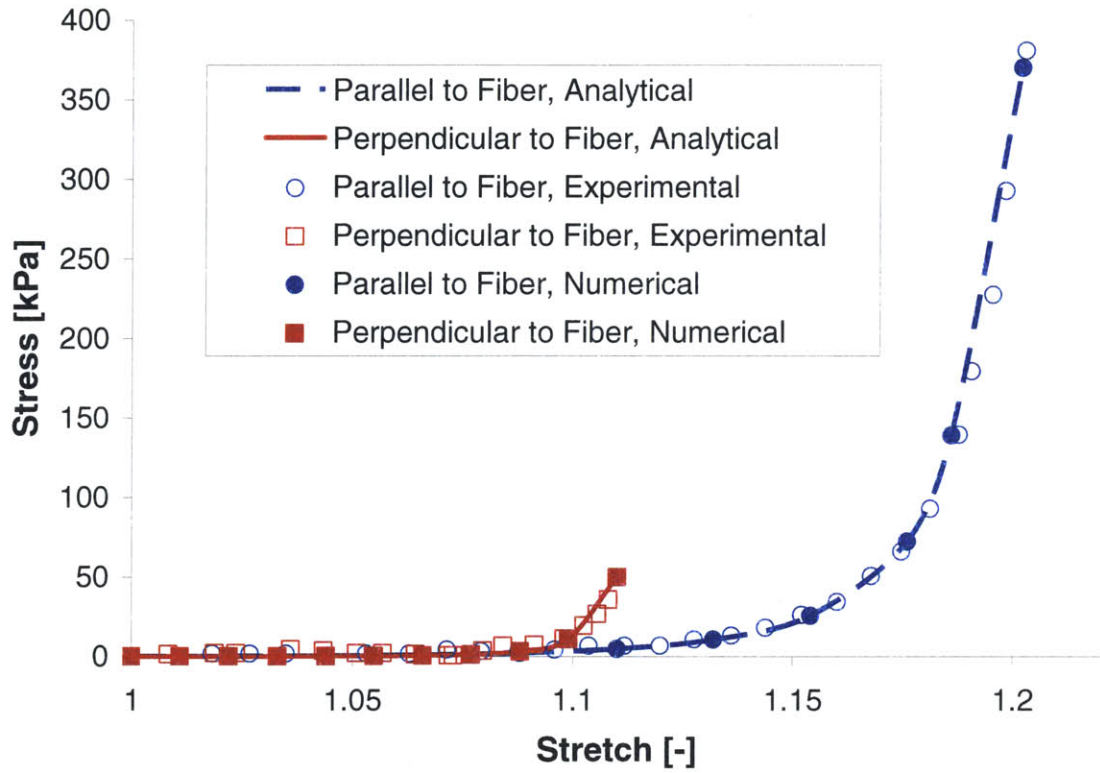


Figure 3.2. 2:1 Off-biaxial strain applied to anterior leaflet

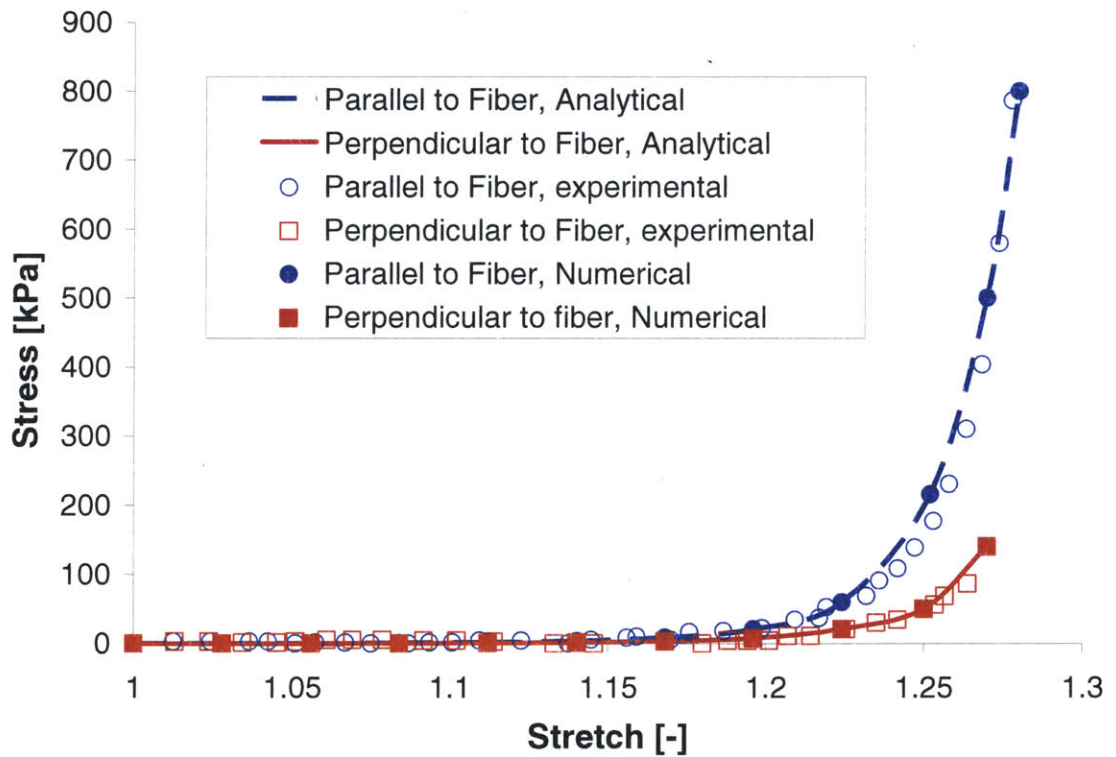


Figure 3.3. Equibiaxial strain applied to posterior leaflet.

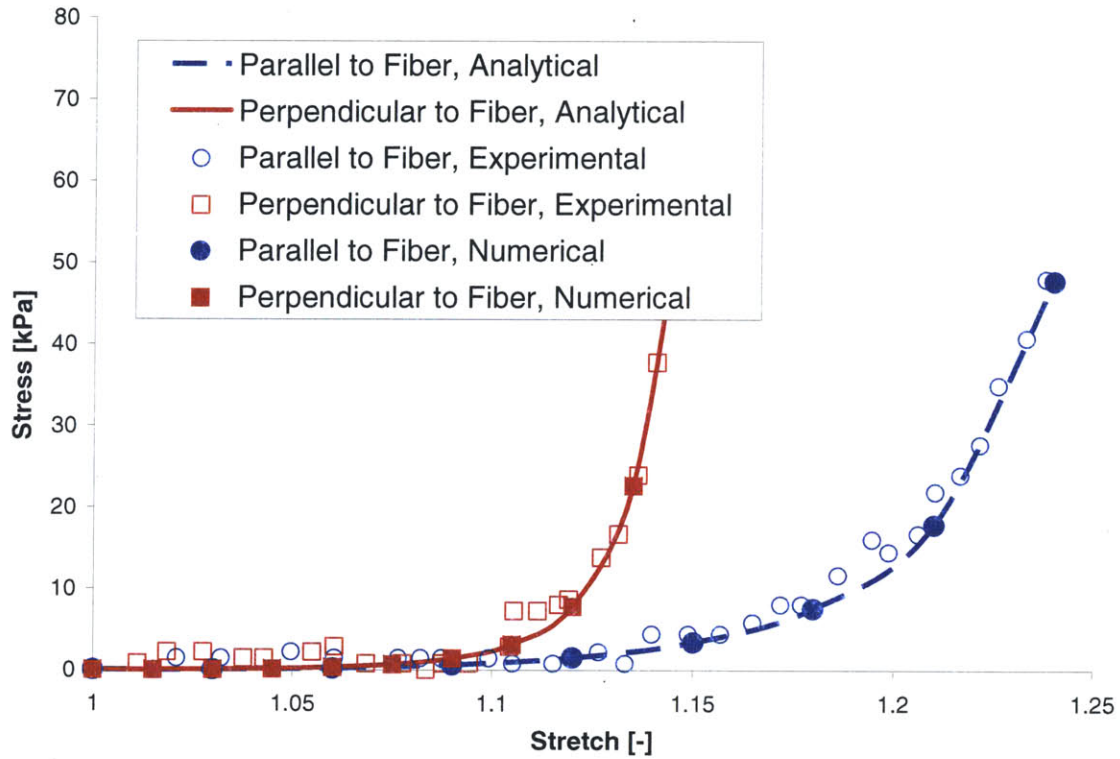


Figure 3.4. 2:1 Off-baxial strain applied to posterior leaflet

In these four cases, the result of the finite element solution matches the analytical solution with errors within the limits of numerical accuracy. The stiffness matrix was positive definite at all steps. Within the stress range of these experiments and at stresses up to 5×10^4 kPa, the volume ratio stayed within $\pm 0.001\%$ of 1, showing that incompressibility was maintained.

3.7. Discussion

Data plotted in Figures 3.1-3.4 show that the numerical implementation accurately represents the analytical solution in biaxial conditions. Adding a term to the strain energy to maintain positive definiteness was effective without introducing significant error to the stresses.

The mixed formulation relies on the volumetric stresses being much larger than the deviatoric in order to enforce incompressibility. Due to the high exponential material behavior, strains just beyond those in the protocols used here can cause deviatoric stresses large enough to affect the incompressibility. Our approach still enforces incompressibility at stresses well beyond those expected in a functioning mitral valve.

3.8. Conclusions

The model presented here is accurate in predicting mitral valve leaflet behavior over the necessary stress range. With use of general 3D elements, this model is applicable to finite-element simulation of mitral valve function.

4. A finite shell element for heart mitral valve leaflet mechanics, with large deformations and 3D constitutive material model

4.1. Introduction

In the previous chapter we present a method for using the constitutive material model for heart mitral valve leaflet tissue with general three-dimensional elements. With the thin-body geometry of the leaflet, accurate results of the bending behavior require a high-order element and fine meshing that exert high computational expense. To handle this simulation more efficiently, we propose here a shell element formulation that includes the 3D constitutive material model.

A 4-node mixed-interpolation shell is formulated in convected coordinates. This shell model is made capable of handling arbitrary three dimensional (3D) material models by use of an algorithm that satisfies the shell stress assumption at every element integration point. Comparison to analytical solutions show this element gives the correct large-deformation behavior for linear-elastic, Mooney-Rivlin, and for a transversely isotropic model specifically for mitral valve leaflet tissue. This element is well-suited to simulating heart valve mechanics, as it is computationally efficient compared to similar methods and can handle the necessary large-deformation dynamic behavior.

In large-deformation shell calculations, the through-thickness strain contributes significantly to the stress response and stiffness tensor. This strain cannot be calculated using the standard interpolations used for other strains, but a variety of ways to calculate the through-thickness strain have been described. 3D shell elements are attractive, in that they generally do not require manipulation of the material model to fit shell stress assumptions (Chapelle, 2004; Sze, 2004). Methods to incorporate a 3D material model into a conventional shell by use of an extensible normal vector have received much attention (Betsch 1996, Simo 1990, Basar 2003). A simpler method to achieve the same has been proposed by Klinkel and Govindjee (Klinkel, 2002). Both conventional shell methods are expected to be cheaper than the 3D shell in our case. The 3D shell model will require significantly more nodes than a conventional shell, particularly requiring

multiple nodes through the thickness to represent bending behavior. Additionally, for an incompressible material like that of mitral leaflet tissue, the 3D shell model will require the added complexity of a mixed pressure-displacement formulation (Sussman, 1987) that the conventional shell will not. We have chosen to use the latter shell method on the basis that it is more computationally efficient than methods involving the extensible normal (Klinkel, 2002).

A 4-node quadrilateral with mixed interpolation of the transverse strains is currently accepted as the most cost-effective shell (Bathe, 1996). This shell is implemented (Dvorkin, 1984a) and the method of Klinkel is used to incorporate the 3D material models. The formulation is verified first with familiar analytical solutions for linear-elastic and Mooney-Rivlin material behavior. Next, the model for leaflet tissue is applied and numerical results are shown to match in-plane analytical results. Out-of plane results are shown and the element is demonstrated in a dynamic case important for simulating heart valve motion.

4.2. Methods

4.2.1. Continuum Mechanics Definitions

The shell calculations are performed in the Green-Lagrange strain tensor,

$$\boldsymbol{\varepsilon} = \frac{1}{2}(\mathbf{F}^T \cdot \mathbf{F} - \mathbf{I}), \quad (4.1)$$

where \mathbf{I} is the identity tensor. Here we restate some of the definitions from previous chapters in terms of the Green-Lagrange strain. The right Cauchy-Green deformation tensor is

$$\mathbf{C} = \mathbf{F}^T \cdot \mathbf{F} = 2\boldsymbol{\varepsilon} + \mathbf{I}, \quad (4.2)$$

and the stress state is calculated from the strain energy function, W , using

$$\mathbf{S} = \frac{\partial W}{\partial \boldsymbol{\varepsilon}} = 2 \frac{\partial W}{\partial \mathbf{C}}, \quad (4.3)$$

where \mathbf{S} is the 2nd Piola-Kirchoff stress tensor. The material constitutive tensor is now

$$\mathbf{C} = \frac{\partial^2 W}{\partial \boldsymbol{\varepsilon}^2} = 4 \frac{\partial^2 W}{\partial \mathbf{C}^2}. \quad (4.4)$$

4.2.2. Constitutive Material Model

A strain-energy function for mitral valve leaflet tissue has been discussed in previous chapters (May-Newman, 1998),

$$W(I_1, I_4) = c_0 \left\{ \exp \left[c_1 (I_1 - 3)^2 + c_2 (I_4^{1/2} - 1)^4 \right] - 1 \right\}, \quad (4.5)$$

with constants for the anterior and posterior leaflet given previously.

As in the previous chapter, a neo-Hookean term is added to avoid the zero matrix at low strains and a volumetric term is added to enforce incompressibility.

$$W(I_1, I_4) = c_0 \left\{ \exp \left[c_1 (I_1 - 3)^2 + c_2 (I_4^{1/2} - 1)^4 \right] - 1 \right\} + c_{PD} (I_1 - 3) + \kappa (\sqrt{I_3} - 1)^2 \quad (4.6)$$

where c_{PD} is a constant chosen to be very small compared to the other effective material moduli and κ is the compressibility, chosen to be a value much higher than any other effective material moduli. This term is the same as that used in the pressure-displacement formulation (Sussman, 1987). The deviatoric and volumetric responses do not have to be isolated from each other in this method. Thus the rest of the modifications to the strain-energy function performed in the mixed formulation in the previous chapter are not necessary.

4.2.3. Shell Element Description

The 4-node shell element with 5 degrees of freedom known as the MITC4 is described in convected coordinates and uses mixed interpolation of the transverse strains to avoid

locking (Dvorkin, 1984a; Dvorkin, 1984b). Here we outline the basis of this formulation. In the global Cartesian coordinate system (e_1, e_2, e_3) , the coordinates (x_1, x_2, x_3) of a particle having natural shell coordinate (r_1, r_2, r_3) is

$${}^t x_i = h_k {}^t x_i^k + \frac{r_3}{2} a_k h_k {}^t V_{ni}^k, \quad (4.7)$$

where x^k is the global position of node k , V_n is the director vector at node k , $h_k(r_1, r_2)$ is the interpolation function corresponding to node k , ${}^t a_k$ is the thickness at node k measured in the direction of V_n at time t . We allow the thickness a_k to vary in time (Dvorkin, 1995) and also recalculate a_k at each time step to reflect changes due to the rotation of V_n .

Throughout, the left superscript t refers to the time and the right subscript i refers to the component in the x_i direction. Local orthogonal vectors are defined:

$${}^0 V_1^k = \frac{\mathbf{e}_2 \times {}^0 V_n^k}{|\mathbf{e}_2 \times {}^0 V_n^k|}, \quad (4.8)$$

$${}^0 V_2^k = {}^0 V_n^k \times {}^0 V_1^k,$$

and the rotation of these vectors in time is achieved by rotation matrix (Argyris, 1982).

The displacement ${}^t u_i$ and incremental displacement u_i are

$${}^t u_i = h_k {}^t u_i^k + \frac{r_3}{2} a_k h_k ({}^t V_{ni}^k - {}^0 V_{ni}^k), \quad (4.9)$$

$$u_i = h_k u_i^k + \frac{r_3}{2} {}^t a_k h_k (-{}^t V_{2i}^k \alpha_k + {}^t V_{1i}^k \beta),$$

where α and β are the rotational degrees of freedom. Covariant base vectors are given by

$${}^t \mathbf{g}_i = \frac{\partial {}^t \mathbf{x}}{\partial r_i} \quad (4.10)$$

and the contravariant base vectors ${}^t \mathbf{g}^i$ are calculated to analytically satisfy ${}^t \mathbf{g}_i \cdot {}^t \mathbf{g}^i = \delta_{ij}$. The Green-Lagrange strains are calculated in the covariant system,

$${}^t \tilde{\mathcal{E}}_{ij} = \frac{1}{2} ({}^t \mathbf{g}_i \cdot {}^t \mathbf{g}_j - {}^0 \mathbf{g}_i \cdot {}^0 \mathbf{g}_j), \quad (4.11)$$

where the tilde overbar denotes values measured in the covariant system.

The stress-strain (Equation 4.3) and constitutive stiffness (Equation 4.4) calculations must be performed in a Cartesian coordinate system. We introduce a particular Cartesian

system for the current application. First the fiber direction N is defined in global coordinates and transformed to covariant coordinates, ${}^t\tilde{N}$, by standard vector transform (Bathe, 1996). In heart valve leaflet tissue, the fiber direction lies in the plane of the leaflet (May-Newman, 1998), so we assume that the fiber direction lies parallel to the element mid-plane. We define a local fiber-aligned Cartesian coordinate system \hat{e} by

$${}^t\hat{e}_1 = \frac{{}^t\tilde{N}}{|{}^t\tilde{N}|}, \quad {}^t\hat{e}_3 = \frac{{}^t\mathbf{g}_1 \times {}^t\mathbf{g}_2}{|{}^t\mathbf{g}_1 \times {}^t\mathbf{g}_2|}, \quad {}^t\hat{e}_2 = {}^t\hat{e}_3 \times {}^t\hat{e}_1, \quad (4.12)$$

where the hat overbar denotes quantities measured in this system. The first direction of this system is parallel to the fiber direction (so that $\hat{N} = [1 \ 0 \ 0]$ at all times), and the third direction is parallel to the through-thickness direction. This coordinate system is convenient to use with the Klinkel method described in the next section.

The Green-Lagrange strains are transformed from the covariant system to the Cartesian local,

$$\hat{\varepsilon}_{ij} = ({}^o\mathbf{g}^i \cdot {}^t\hat{e}_m) ({}^o\mathbf{g}^j \cdot {}^t\hat{e}_n) \tilde{\varepsilon}_{mn}. \quad (4.13)$$

The constitutive material tensor in the local Cartesian coordinate system is denoted $\hat{\mathbf{C}}$, which contains the shell assumption of zero stress in the through-thickness direction. For nonlinear materials, this tensor may be calculated as in Equation 4.4 using the Green-Lagrange strain in Cartesian coordinates from Equation 4.13. In the case of linear elasticity $\hat{\mathbf{C}}$ is constant. The constitutive tensor is made to relate the incremental covariant strains to the incremental contravariant stresses by the transformation

$$\tilde{\mathbf{C}}^{ijkl} = ({}^t\mathbf{g}^i \cdot \hat{e}_m) ({}^t\mathbf{g}^j \cdot \hat{e}_n) ({}^t\mathbf{g}^k \cdot \hat{e}_o) ({}^t\mathbf{g}^l \cdot \hat{e}_p) \hat{\mathbf{C}}^{mnop}. \quad (4.14)$$

In linear elasticity, the contravariant stresses can be calculated by:

$$\tilde{S}^{ij} = \tilde{\mathbf{C}}^{ijkl} \tilde{\varepsilon}_{kl}. \quad (4.15)$$

For nonlinear materials, the stresses are calculated in the local Cartesian coordinates as in (Equation 4.3), then transformed to the covariant coordinates,

$$\tilde{S}^{ij} = ({}^t\hat{e}_m \cdot {}^t\mathbf{g}^i) ({}^t\hat{e}_n \cdot {}^t\mathbf{g}^j) \hat{S}_{mn}. \quad (4.16)$$

All strain components are computed in the standard manner (Bathe, 1996), except for the transverse shear strains which are found using separate interpolations to avoid locking:

$$\begin{aligned} \tilde{\epsilon}_{13}(r_1, r_2, r_3) &= \frac{1}{2}(1+r_2)\tilde{\epsilon}_{13}\Big|_A + \tilde{\epsilon}_{13}(r_1, r_2, r_3) = \frac{1}{2}(1-r_2)\tilde{\epsilon}_{13}\Big|_C, \\ \tilde{\epsilon}_{23}(r_1, r_2, r_3) &= \frac{1}{2}(1+r_1)\tilde{\epsilon}_{23}\Big|_D + \tilde{\epsilon}_{23}(r_1, r_2, r_3) = \frac{1}{2}(1+r_1)\tilde{\epsilon}_{23}\Big|_B, \end{aligned} \quad (4.17)$$

where A is the location ($r_1=0, r_2=1, r_3=0$), B is ($r_1=-1, r_2=0, r_3=0$), C is ($r_1=0, r_2=-1, r_3=0$), and D is ($r_1=1, r_2=0, r_3=0$).

In a Total Lagrangian formulation with convected coordinates, the linearized equation of motion is

$$\int_{{}^0V} {}^0\tilde{\mathbf{C}}^{ijkl} {}^0\tilde{\epsilon}_{kl} \delta_0 \tilde{\epsilon}_{ij} {}^0 dV + \int_{{}^0V} {}^t\tilde{S}^{ij} \delta_0 \tilde{\eta}_{ij} {}^0 dV = {}^{t+\Delta t}\mathfrak{R} - \int_{{}^0V} {}^t\tilde{S}^{ij} \delta_0 \tilde{\epsilon}_{ij} {}^0 dV, \quad (4.18)$$

where $\tilde{\epsilon}_{ij}$ and $\tilde{\eta}_{ij}$ are the linear and nonlinear parts of the Green-Lagrange strain components $\tilde{\epsilon}_{ij}$ (Dvorkin, 1984b). All terms are calculated using the above definitions.

For use in dynamic simulations, the mass matrix is

$$\int_{{}^0V} \rho \mathbf{H}^T \mathbf{H} d{}^0V, \quad (4.19)$$

where H is the matrix of interpolation functions (Bathe, 1996).

4.2.4. Local Plane-Stress Algorithm for Calculation of Stresses and Constitutive Tensor

In the MITC shell formulation, the stresses and material stiffness tensor needed to compute the finite element matrices must reflect the stress assumption of zero through-thickness stress. Klinkel and Govinjee provide a simple, rigorous method for incorporating an arbitrary 3D material model into a shell element (Klinkel, 2002). They refer to this method as the local plane stress algorithm. In this method, the stress vector, strain vector, and stiffness tensor are partitioned:

$$\begin{bmatrix} \partial \hat{S}_m \\ \partial \hat{S}_z \end{bmatrix} = \begin{bmatrix} \hat{\mathbf{C}}_{mm} & \hat{\mathbf{C}}_{mz} \\ \hat{\mathbf{C}}_{zm} & \hat{\mathbf{C}}_{zz} \end{bmatrix} \begin{bmatrix} \partial \hat{\epsilon}_m \\ \partial \hat{\epsilon}_z \end{bmatrix}, \quad (4.20)$$

where, for the shell, we have the definitions

$$\hat{\mathbf{S}}_m = \begin{bmatrix} \hat{S}_{11} & \hat{S}_{12} & \hat{S}_{13} & \hat{S}_{22} & \hat{S}_{13} \end{bmatrix}^T, \quad \hat{S}_z = \hat{S}_{33}. \quad (4.21)$$

The stress, strain, and stiffness components here are those in the fiber-aligned Cartesian system defined by Equation 4.12. The following are the steps of the plane stress algorithm incorporated into the shell model. This routine is run for each integration point in each iteration.

1. The Green-Lagrange strains $\hat{\epsilon}$, not including the through-thickness strain, are calculated in the local Cartesian system by Equations 4.11 and 4.13.

2. An initial guess is made for the through-thickness strain $\hat{\epsilon}_{33}$. We use the value of $\hat{\epsilon}_{33}$ from the previous converged iteration for this guess.

2. The second Piola-Kirchoff stresses $\hat{\mathbf{S}}$ and material stiffness tensor $\hat{\mathbf{C}}$ are calculated by applying Equations 4.3 and 4.4, respectively to the strain energy function (Equation 4.5), with the fiber direction $\hat{\mathbf{N}} = [1 \ 0 \ 0]$.

3. If $\|\hat{S}_z\|$ is larger than a chosen tolerance, the through-thickness strain is updated by

$$\hat{\epsilon}_z^{i+1} = \hat{\epsilon}_z^i - \frac{\hat{S}_z^i}{\hat{\mathbf{C}}_{zz}^i} \quad (4.22)$$

and the method is returned to step 2. If the $\|\hat{S}_z\|$ is smaller than a chosen tolerance, the algorithm continues to step 4.

4. With $\hat{S}_z = 0$, the stiffness matrix can be condensed using

$$\hat{\mathbf{C}}_{condensed} = \begin{bmatrix} \hat{\mathbf{C}}_{mm} - \frac{1}{\hat{\mathbf{C}}_{zz}} \hat{\mathbf{C}}_{mz} \hat{\mathbf{C}}_{zm} \end{bmatrix}. \quad (4.23)$$

5. A row and column of zeros are inserted into $\hat{\mathbf{C}}_{condensed}$ to represent the through-thickness direction, yielding the stiffness matrix with shell assumption $\hat{\mathbf{C}}$ in the local

Cartesian system. At this step, the stresses $\hat{\mathbf{S}}$ are the stresses in the local fiber-aligned Cartesian system, with the through-thickness stress equal to zero within the chosen tolerance.

The stiffness tensor is then transformed to the natural shell coordinate system using Equation 4.14, and the stresses are transformed to the covariant system by Equation 4.16. Thus the stiffness tensor and stresses from a 3D constitutive model are incorporated into our shell.

4.3. Numerical Tests and Results

We have implemented our element in the commercially available finite element software ADINA (Watertown, MA), using 2x2x2 Gauss integration for all terms. Here we describe a series of tests on the implemented element.

First we verify that the element behavior matches well-known analytical solutions with and without the plane-stress iteration. A shell is subjected to stretching in one in-plane direction while unconstrained in the other in-plane direction. The shell with linear elastic material model and no plane stress iteration was compared to analytical plane strain solution. The shell with linear elastic material model and plane stress iteration was compared to analytical uniaxial stress solution. The stress-stretch behavior exhibited by a shell model with single-term incompressible Mooney-Rivlin (neo-Hookean) material was compared to analytical uniaxial stress solution (Figure 4.1). In these cases, the numerical results matched the analytical within the limits of numerical accuracy.

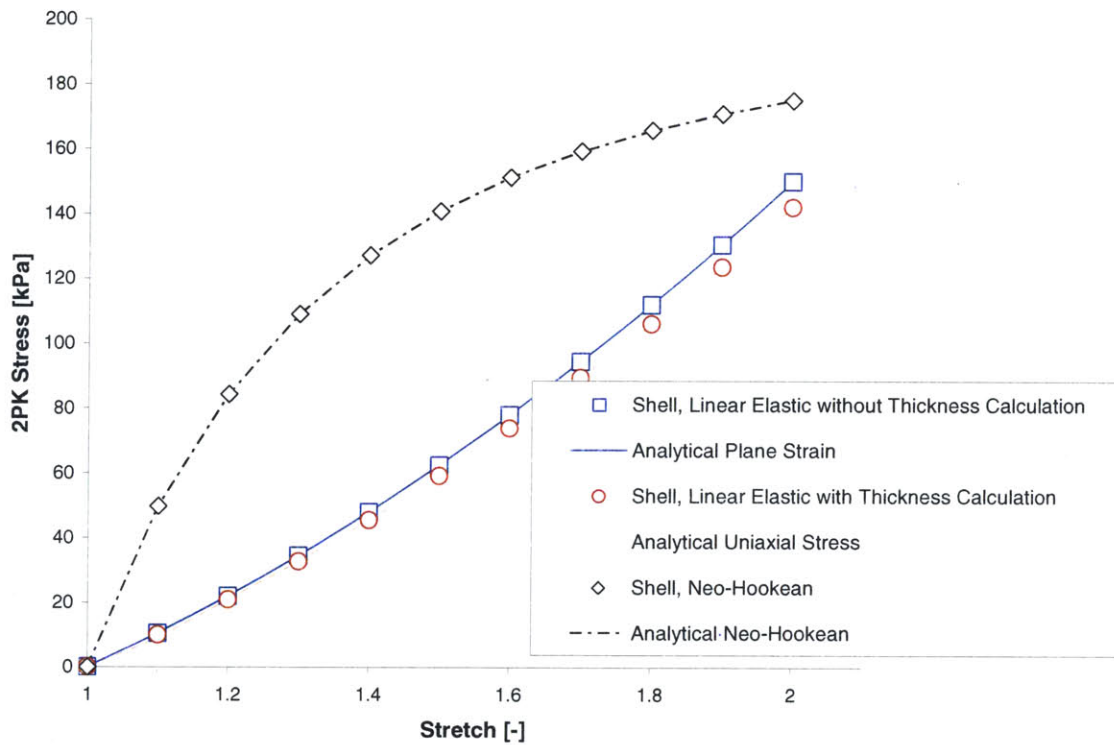


Figure 4.1. Numerical and analytical solutions for uniaxial stretching. Linear elastic model with $E=100$, $\nu=0.3$; Neo-Hookean with $C=100$, $\kappa=1e5$.

The next test case is to compare the full model, with strain-energy function for mitral valve mechanics and plane-stress iteration, to planar analytical results. Equibiaxial stretch was applied to the element with the material models for anterior and posterior leaflets. The range of deformations here is the same as that in the May-Newman and Yin data (1998), which reflects the range of deformations expected in physiological leaflet function. The numerical results (see Figures 4.2 and 4.3) match the analytical within the limits of numerical accuracy.

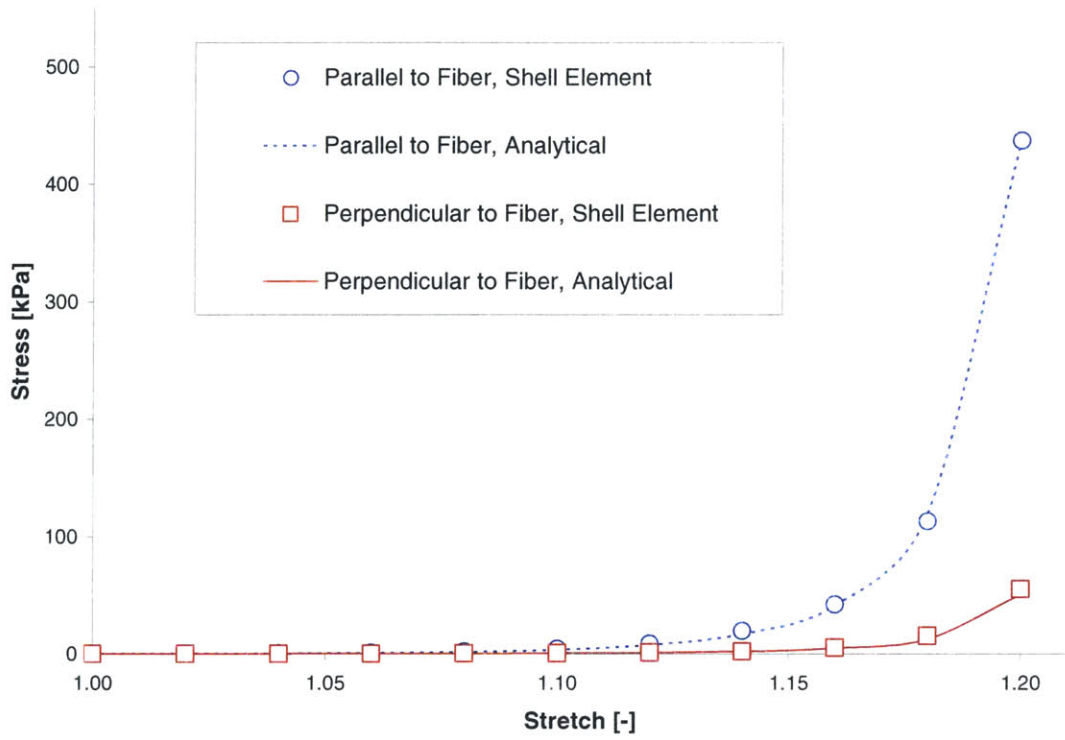


Figure 4.2. Numerical and analytical results for equibiaxial stretching of anterior leaflet

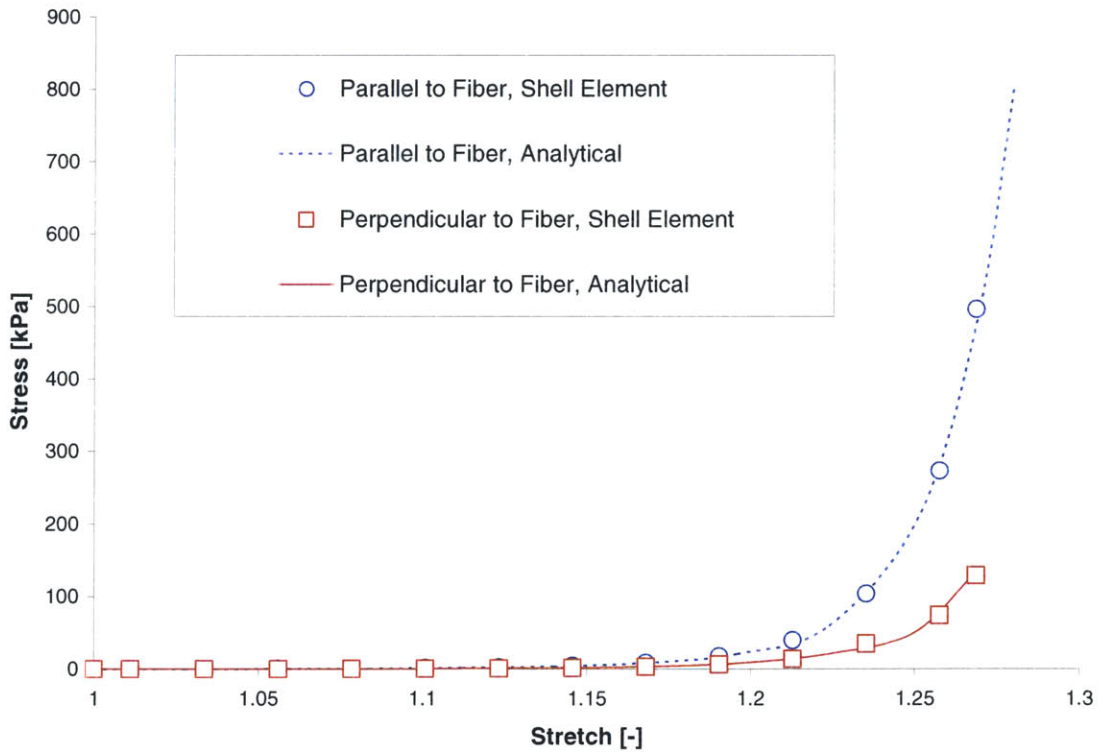


Figure 4.3. Numerical and analytical results for equibiaxial stretching of posterior leaflet

The element is further tested in cantilever bending, with an applied tip rotation. Results of the moment versus applied tip rotation for the anterior and posterior leaflet, with the rotation applied parallel to the fiber direction and perpendicular to the fiber direction, are plotted in Figure 4.4. Dimensions are typical of a piece of leaflet tissue: 1cm square with a thickness of 0.45mm. The element is converged to tip rotations of $\pi/2$. Exponential material behavior is seen in the moment, and the directional behavior is seen as both leaflets are stiffest in the direction parallel to the fiber.

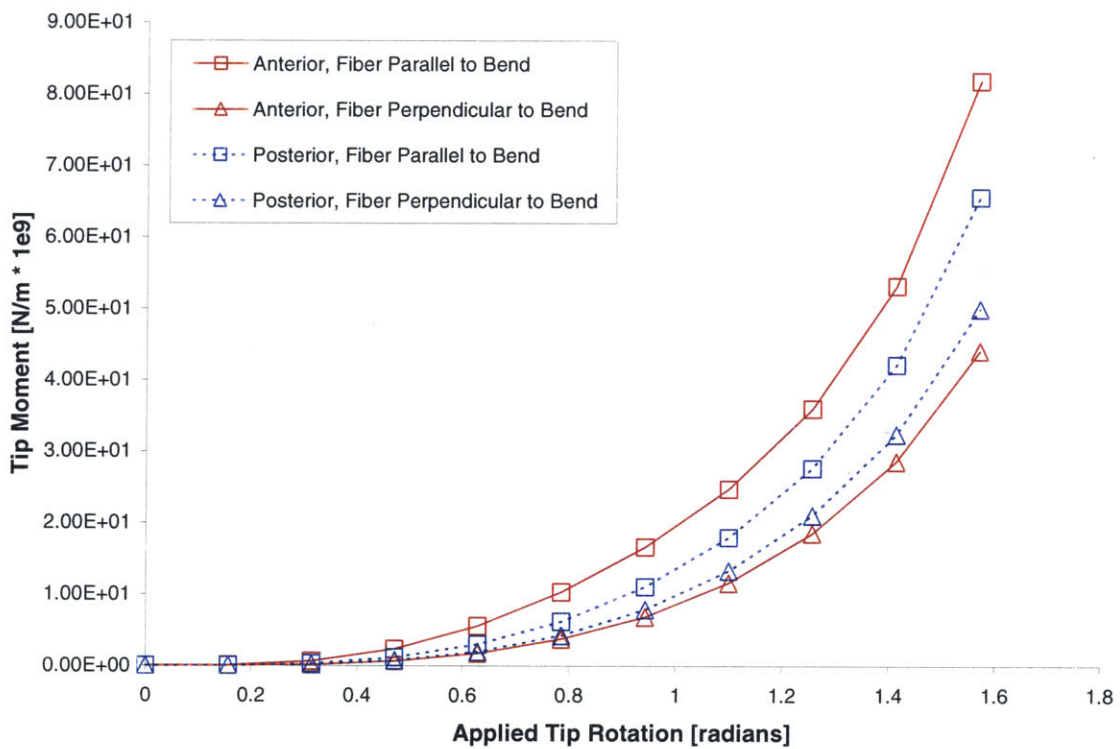


Figure 4.4. Moment versus applied rotation at tip of cantilevered element, for anterior and posterior leaflet materials with bending parallel and perpendicular to fiber direction.

Our final test case is to verify that the element can represent physical situations typical of leaflet motion. Particularly, leaflets are pushed through changes in curvature by dynamic forces. Here, we apply a pressure to a curved shell to push the shell through its snap point, and let the inertia of the shell control the snapping. A curved body having length of 3mm, width of 1mm, and thickness of 0.45mm is meshed with three elements. We use the anterior leaflet material model with a density of 10kg/m^3 . A time-varying pressure is

applied to the outer surface of the body. The initial and final configurations of the leaflet model are shown in Figure 4.5. To further quantify the behavior of the model through the snap motion, we examined the displacement of the shell apex and applied pressure versus time (see Figure 4.6). As evident in the figures, the shell model passes through the snap point and settles in the opposite stable position.

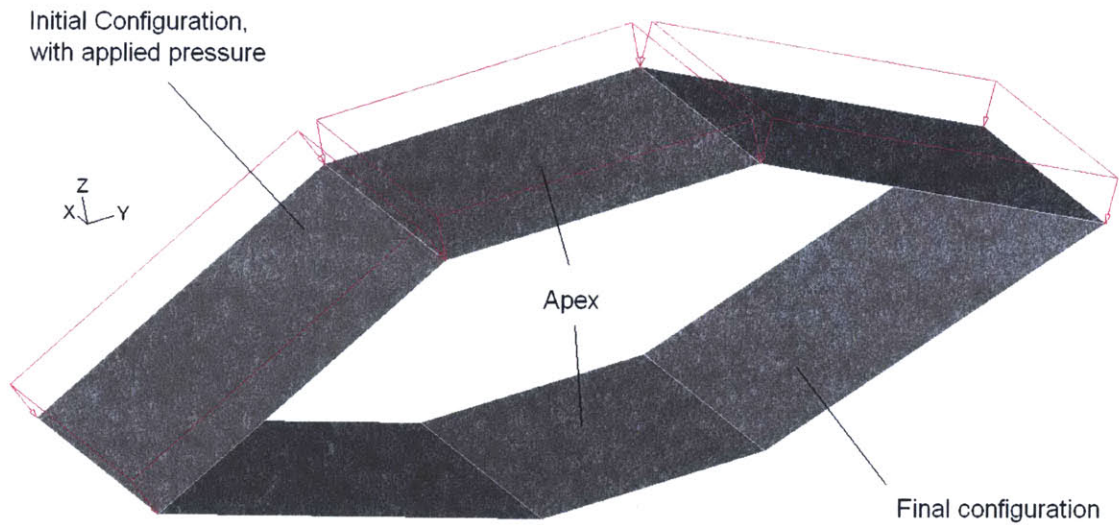


Figure 4.5. Initial and final geometry in dynamic snapping test.

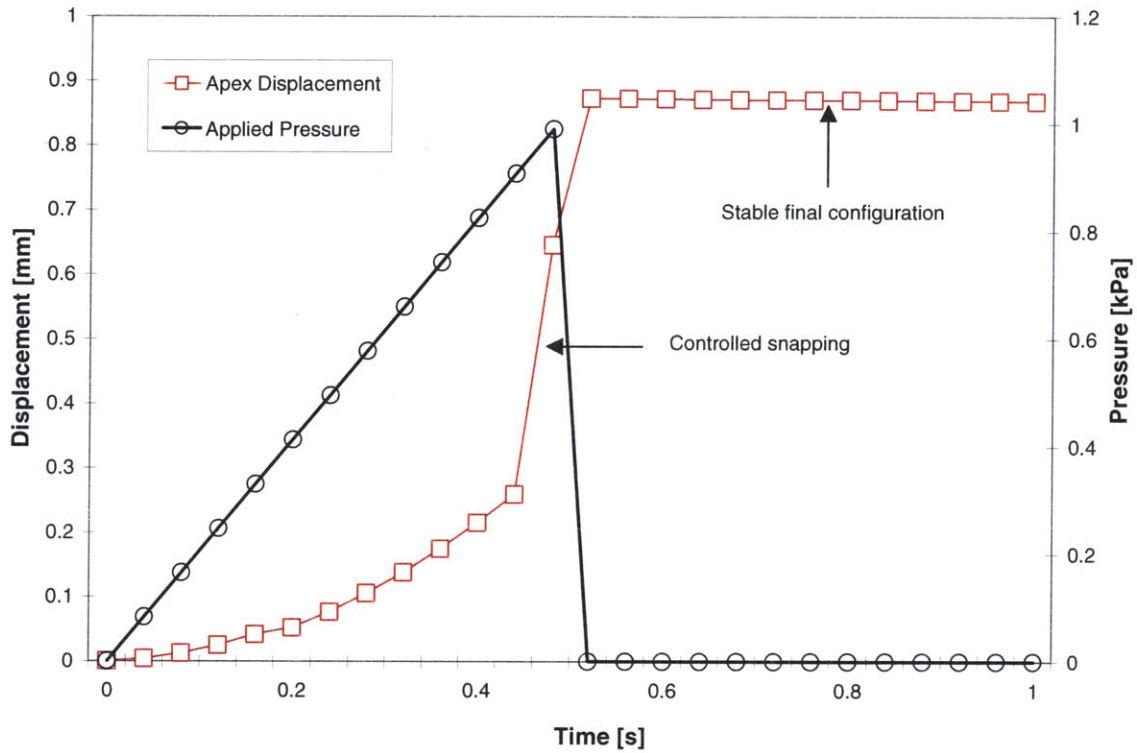


Figure 4.6. Applied pressure and resulting displacement versus time for dynamic snapping test.

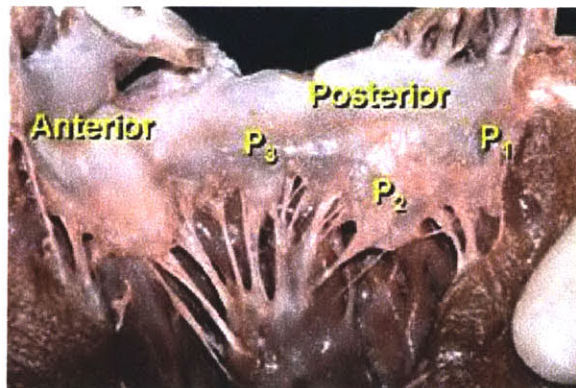
4.4. Conclusions

A shell model appropriate for simulation of heart mitral valve leaflet motion has been presented. This model combines three rigorously derived parts: the MITC4 shell element, a 3D constitutive model for the tissue, and the plane stress iteration for incorporating a 3D material into the shell. Here we have shown that our element combining these parts is effective and accurate in modeling large deformations. The element is accurate in matching analytical solutions and can represent the dynamic curvature changes found in leaflet motion. This shell element models the tissue with a 4-node shell, achieving a radical savings in computational expense over the method using a 27-node mixed-interpolation solid element presented in the previous chapter. Promising future applications of this element include finite element simulations of mitral valve function, examination of the bending behavior of leaflet tissue, and extension to include the layered histology of the leaflet.

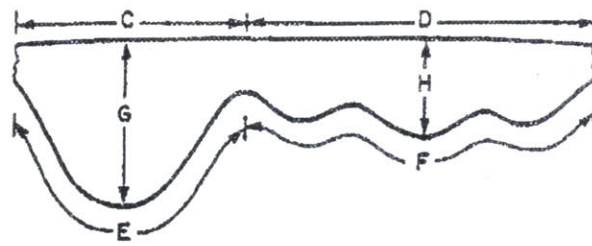
5. Conclusions and Future Directions

This thesis presents methods for applying a three-dimensional material model for heart mitral valve mechanics in finite elements. Mitral valve physiology, ailments, and treatments are outlined in the context of motivation for development of a new hybrid synthetic/tissue engineered mitral valve replacement. The usefulness of numerical modeling of the mitral valve to this effort and to general understanding of mitral valve is discussed. A review is given of analytical constitutive modeling for heart valve leaflet tissue. An invariant-based strain energy function for mitral valve leaflet tissue mechanics is selected for numerical implementation. The novel work of this thesis is two implementations of this strain energy function. A mixed pressure-displacement formulation is used to implement the material model in general three-dimensional finite elements. A shell model is formulated that includes the three-dimensional material behavior by use of a local plane stress iteration. These two implementations are valuable to mitral valve research: either can serve as the basis for the solid phase of a finite element simulation of the valve.

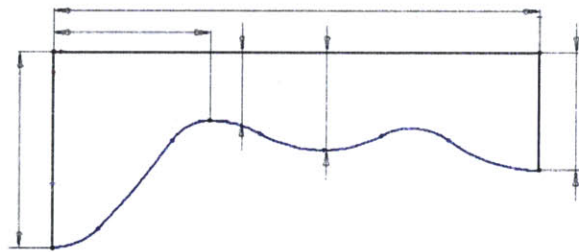
The immediate use of this model is application in finite element modeling of the normal mitral valve. We have prepared the geometry of the normal mitral valve in finite elements for both the 3D and shell elements. The geometry of the flattened geometry has been measured (Kunzelman, 1994), and we have drawn this geometry in CAD software (Solidworks Corporation, Concord MA) as shown in Figure 5.1.



(a)



(b)



(c)

Figure 5.1. Normal mitral valve flattened (a) (Echo In Context, 2005), characteristic dimensions of explanted mitral valve leaflets (Kunzleman, 1994), and CAD representation of mitral valve leaflet geometry (c).

Once the leaflet geometry has been generated, it is given a thickness and wrapped around the shape of the mitral orifice to give a three dimensional body with shape representative of the mitral leaflets close to their zero-stress state. This body is imported into the finite element software (ADINA, Watertown, MA) and then meshed with either three-dimensional or shell elements. Chordae are represented by nonlinear spring elements. The body meshed with three-dimensional elements is shown in Figure 5.2.

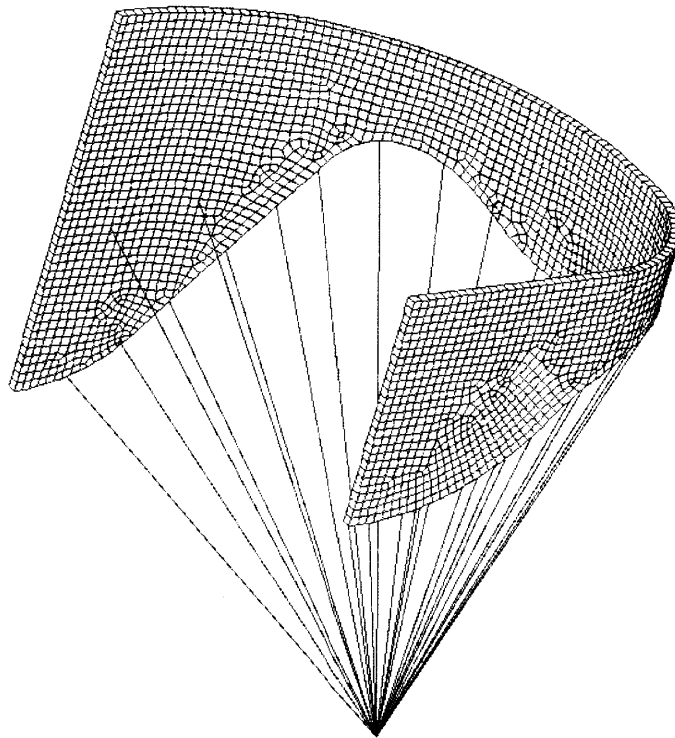


Figure 5.2. Mitral valve geometry meshed with three-dimensional elements

Boundary conditions are taken from physiological observations. Beating of the heart muscles applies a time-varying contraction to the mitral annulus and a displacement of the point where all of the chordae meet (the papillary muscle). The fluid can be represented simply as a pressure boundary condition on the leaflet surface (Kunzelman, 1993) or full fluid-structure interaction can be incorporated (Einstein, 2004). We are currently implementing these conditions to create a complete model of the healthy mitral valve that we can verify against dynamic measurements from human valves (Levine, 1989). The next step will be to include the synthetic materials, for which the numerical models presented in this thesis can be applied, to evaluate hybrid designs. The model can also be used to evaluate physical mechanisms of valvular diseases.

Other significant directions for future work include further refinements of the formulations presented here and extension to other tissues. The most notable refinement would be to examine the assumption that the leaflet tissue is homogenous through its thickness. While leaflets comprised of three distinct layers, all models yet presented

assume homogeneity of the tissue. A model including the effects of the layers would help elucidate the function of the multiple layers. The shell formulation can be readily extended to multilayer behavior by inclusion of additional integration points through the thickness and allowing the material constitutive tensor to vary through the thickness. This does not require additional meshing through the thickness, and thus does not represent a large computational expense. Additional refinements should include experimental verification of the model in deformation states other than biaxial tension and determination of the effects of the ridged histology of the leaflet on its stress-deformation behavior.

References

- Almeida E.S., Spilker R.L. 1998. Finite element formulations for hyperelastic transversely isotropic biphasic soft tissues. *Computer Methods in Applied Mechanics and Engineering*. 151:513-538.
- Argyris JH. 1982. An excursion into large rotations. *Computer Methods in Applied Mechanics and Engineering*. 32: 85-155.
- Arts T, Meerbaum S, et al. 1983. Stresses in the closed mitral valve: a model study. *Journal of Biomechanics*. 7: 539-547.
- Basar Y, Hanskotter U, et al. 2003. A general high-order finite element formulation for shells at large strains and finite rotations. *International Journal for Numerical Methods in Engineering*. 57: 2147-2175.
- Bathe, K.J. 1996. *Finite element procedures*. Prentice Hall: New Jersey.
- Betsch P, Gruttmann F, et al. 1996. A 4-node finite shell element for the implementation of general hyperelastic 3d-elasticity at finite strains. *Computer Methods in Applied Mechanics and Engineering*. 130: 57-79.
- Billiar KL and Sacks MS. 2000. Biaxial mechanical properties of the natural and glutaraldehyde treated aortic valve cusp- Part I: Experimental results. *Journal of Biomechanical Engineering*. 122: 23-30.
- Billiar KL and Sacks MS. 2000. Biaxial mechanical properties of the native and glutaraldehyde-treated aortic valve cusp: Part II- A structural constitutive model. *Journal of Biomechanical Engineering*. 122: 327-335.
- Bischoff JE, Arruda EA, et al. 2002 microstructurally based orthotropic hyperelastic constitutive law. *Journal of Applied Mechanics*. 69: 570-579.
- Bloomfield P, Wheatley DJ, et al. 1991. Twelve-year comparison of Bjork-Shiley mechanical heart valve with porcine bioprosthesis. *New England Journal of Medicine*. 324: 573-579.
- Booth C, Korossis SA, et al. 2002. Tissue engineering of cardiac valve prosthesis I: development and histological characterization of an acellular porcine scaffold. *Journal of Heart Valve Disease*. 11: 457-462.
- Boyce MC and Arruda EA. 2000. Constitutive models of rubber elasticity: A review. *Rubber Chemistry and Technology*. 73(3): 504-523.
- Broom D. 1978. Simultaneous morphological and stress-strain studies of the fibrous components in wet heart valve leaflet tissue. *Connective Tissue Research*. 6: 37-50.
- Butany J, Ahluwalia MS, et al. 2003. Mechanical heart valve prostheses: identification

- and evaluation. *Cardiovascular Pathology*. 12(6): 322-344.
- Butany J, D'Amati G, et al. 1990. Detailed examination of complete bioprosthetic heart valves. *ASAIO Transactions*. 36: M414-M417.
- Carew T.E., Vasishnav R.N., and Patel D.J. 1968. Compressibility of the arterial wall. *Circulation Research*. 23: 61-68.
- Carew EO, Talman EA, Boughner DR, et al. 1999. Quasi-linear viscoelastic theory applied to internal shearing of porcine aortic valve leaflets. *Journal of Biomechanical Engineering*. 121: 386-392.
- Chapelle D, Ferent A, et al. 2004. 3D-shell elements and their underlying mathematical model. *Mathematical Models and Methods in Applied Sciences*. 14(1) 105-142.
- Choi HS and Vito RP. 1990. Two-dimensional stress-strain relationship for canine pericardium. *Journal of Biomechanical Engineering*. 112(2): 153-159.
- Clark RE. 1973. Stress-strain characteristics of fresh and frozen human aortic and mitral leaflets and chordae tendinae: implications for clinical use. *Journal of Thoracic and Cardiovascular Surgery*. 66(2): 202-208.
- Deac RF, Simionescu D, et al. 1995. New evolution in mitral physiology and surgery: mitral stentless pericardial valve. *Annals of Thoracic Surgery*. 60: S433-S438.
- DiSilvestro MR, Zhu QL, et al. 2001. Biphasic poroviscoelastic simulation of the unconfined compression of articular cartilage- Simultaneous prediction of reaction force and lateral displacement. *Journal of Biomechanical Engineering*. 123(2): 191-197.
- Dvorkin EN. 1984. On nonlinear finite element analysis of shell structures. PhD Thesis, Department of Mechanical Engineering, Massachusetts Institute of Technology.
- Dvorkin, EN and Bathe KJ. 1984. A continuum mechanics based four-node shell element for general non-linear analysis. *Engineering Computations*. 1: 77-88.
- Dvorkin EN, Pantuso D, and Repetto EA. 1995. A formulation of the MITC4 shell element for finite strain elasto-plastic analysis. *Computer Methods in Applied Mechanics and Engineering*. 125: 17-40.
- Echo In Context. [online] URL: http://www.echoincontext.com/learn_anat.asp [cited May 25, 2005].
- Edwards Lifesciences. [online] URL: <http://www.edwards.com/Products/PorcineValves/Aortic.htm> [cited May 25, 2005].
- Einstein DR, Kunzelman KS, et al. 2004. Haemodynamic determinants of the mitral valve closure sound: a finite element study. *Medical & Biological Engineering &*

- Computing, 42: 832-846.
- Fuchs JR, Nasser BA, Vacanti JP. 2001. Tissue engineering: a 21st century solution to surgical reconstruction. *Annals of Thoracic Surgery*. 71: 577-591.
- Fung YC. 1967. Elasticity of soft tissues in simple elongation. *American Journal of Physiology*. 213(6): 1532-1544.
- Fung YC. 1993. *Biomechanics: Mechanical properties of living tissues*. Springer-Verlag, New York.
- Gahmbir, S, Ed. *Nuclear Medicine Mediabook*. [online] URL: <http://www.crump.ucla.edu/NM-Mediabook> [cited May 25, 2005].
- Gleason TG, Tirone ED, et al. 2004. St. Jude Medical Toronto biologic aortic root prosthesis: Early FDA phase II IDE study results. *Annals of Thoracic Surgery*. 78(3): 786-793.
- Hart JD, Peters GWM, et al. 2003. A three-dimensional computational analysis of fluid-structure interaction in the aortic valve. *Journal of Biomechanics*. 36:103-112
- Hayashi K. 1994. Fatigue properties of segmented polyether polyurethanes for cardiovascular applications. *Biomaterials' Mechanical Properties, ASTM STP 1173*, Kambic HE and Yokobori, Jr. AT, Eds. American Society for Testing and Materials, Philadelphia. 9-18.
- Hoerstrup SP, Kadner A, et al. 2002. Tissue engineering of functional trileaflet heart valves from human marrow stromal cells. *Circulation*. 106: I143-I150.
- Holzapfel GA. 2001. *Nonlinear solid mechanics: A continuum approach for engineering*. Wiley: New York.
- Holzapfel GA, Eberlein R, et al. 1996. Large strain analysis of soft biological membranes: formulation and finite element analysis. *Computer Methods in Applied Mechanics and Engineering*. 132: 45-61.
- Humphrey JD, Strumpf RK, et al. 1990. Determination of a constitutive relation for passive myocardium: I. A new functional form. *Journal of Biomechanical Engineering*. 112: 333-9.
- Humphrey JD and Yin FCP. 1987. On constitutive relations and finite deformations of passive cardiac tissue: I. A pseudostrain-energy function. *Journal of Biomechanical Engineering*. 109: 298-304.
- Humphrey JD and Yin FCP. 1989. Biomechanical experiments on excised myocardium: theoretical considerations. *Journal of Biomechanics*. 22(4): 377-383.

- Hvidberg E. 1960. Investigations into the effect of mechanical pressure on the water content of isolated skin. *Acta Pharmac.* 16: 245-259.
- Klinkel S, Govindjee S. 2002. Using finite strain 3D-material models in beam and shell elements. *Engineering Computations.* 19(8): 902-921.
- Kominar V, Narkis M, et al. 1995. Compressive strength of unidirectional and crossply carbon fibre/PEEK composites. *Journal of Materials Science.* 30(10): 2620-2627.
- Kunzelman KS, Cochran RP, et al. 1993. Finite element analysis of the mitral valve. *Journal of Heart Valve Disease.* 2:326-340.
- Kunzelman K.S., Cochran R.P., et al. 1993. Finite-element analysis of mitral-valve pathology. *Journal of Long-Term Effects of Medical Implants.* 3(3): 161-170.
- Kunzelman KS, Cochran RP, et al. 1994. Anatomic basis for mitral valve modeling. *Journal of Heart Valve Disease.* 3: 491-496.
- Kunzelman KS, Cochran RP. 1990. Mechanical properties of basal and marginal mitral valve chordae tendinae. *ASAIO Transactions.* 36: M405-M408.
- Kunzelman KS, Reimink MS, et al. 1998. Flexible versus rigid ring annuloplasty for mitral valve annular dilation: a finite element model. *Journal of Heart Valve Disease.* 7: 108-116.
- Lanir Y. 1979. A structural theory for the homogeneous biaxial stress-strain relationships in flat collagenous tissues. *Journal of Biomechanics.* 12: 423-436.
- Lanir Y. 1982. Constitutive equations for fibrous connective tissues. *Journal of Biomechanics.* 16(1): 1-12.
- Laube HR and Matthäus M. 2001. A new semi-automatic endothelial cell seeding technique for biological prosthetic heart valves. *International Journal of Artificial Organs.* 23: 243-246.
- Lee GC, Tseng NT. 1982. Finite element analyses in soft tissue mechanics. *Finite Elements in Biomechanics.* John Wiley & Sons, Ltd, New Jersey.
- Levine RA, Handschumacher MD, et al. 1989. 3-Dimensional echocardiographic reconstruction of the mitral-valve, with implications for the diagnosis of mitral-valve prolapse. *Circulation.* 80(3): 589-598.
- Li J, Luo XY, et al. 2001. A nonlinear model for porcine aortic heart valves. *Journal of Biomechanics.* 34: 1279-89.
- May-Newman K, Yin FCP. 1995. Biaxial mechanical behavior of excised porcine mitral valve leaflets. *American Physiological Society.* 269: H1319-27.

- May-Newman K and Yin FCP. 1998. A constitutive law for mitral valve tissue. *Journal of Biomechanical Engineering*. 120: 38-46.
- Miller GE, Marcotte H. 1987. Computer simulation of human mitral valve mechanics and motion. *Computational Biology and Medicine*. 17(5): 305-319.
- Niwaya K, Knott-Craig CJ, et al. Cryopreserved homograft valves in the pulmonary position: risk analysis for intermediate-term failure. 117: 141-147.
- Obadia JF, Casali C, Chassignolle et al. 1997. Mitral subvalvular apparatus: different functions of primary and secondary chordae. *Circulation*. 96: 3124-3128.
- Perry TE, Kaushal S, et al. 2003. Bone marrow as a cell source for tissue engineering heart valves. *Annals of Thoracic Surgery*. 75: 761-767.
- Reimink MS, Kunzelman KS, et al. 1996. The effect of chordal replacement suture length on function and stresses in repaired mitral valves: a finite element study. *Journal of Heart Valve Disease*. 5:365-375.
- Roberts WC. 1983. Morphologic features of the normal and abnormal mitral valve. *American Journal of Cardiology*. 51: 1005-1028.
- Rousseau EP, Sauren AA, et al. 1983. Elastic and viscoelastic material behaviour of fresh and glutaraldehyde-treated porcine aortic valve tissue. *Journal of Biomechanics*. 16(5): 339-348.
- Rusted IE, Scheifley CH, et al. 1952. Studies of the mitral valve: anatomic features of the normal mitral valve and associated features. *Circulation*. 6: 825-831.
- Rüter M., Stein E. 2000. Analysis, finite element computation and error estimation in transversely isotropic nearly incompressible finite elasticity. *Computer Methods in Applied Mechanics and Engineering*. 190: 519-541.
- Sacks M.S. 2003. Incorporation of experimentally-derived fiber orientation into a structural constitutive model for planar collagenous tissues. *Journal of Biomechanical Engineering*. 125: 280-287.
- Sacks M.S., Sun W. 2003. Multiaxial behavior of biological materials. *Annual Review of Biomedical Engineering*. 5: 251-284.
- Sauren AA, van Hout MC, et al. 1983. The mechanical properties of porcine aortic valve tissues. *Journal of Biomechanics*. 16(5): 327-337.
- Sacks MS. 2003. Incorporation of experimentally-derived fiber orientation into a structural constitutive model for planar collagenous tissues. *Journal of Biomechanical Engineering*. 125: 280-287.

- Schoen FJ, Levy RJ, and Piehler HR. 1991. Pathological considerations in replacement cardiac valves. *Cardiovascular Pathology*. 1(1): 29-52.
- Schoen FJ, Levy RJ. 1999. Tissue heart valves: current challenges and future research perspectives. *Journal of Biomedical Material Research*. 47:439-465.
- Schröder J., Neff P. 2003. Invariant formulation of hyperelastic transverse isotropy based on polyconvex free energy functions. *International Journal of Solids and Structures* 40: 401-445.
- Shinoka T, Ma PX, et al. 1996. Tissue-engineered heart valves: autologous valve leaflet replacement study in a lamb model. 94: III164-III168.
- Shumacker, HB. 1992. *The Evolution of Cardiac Surgery*. Indiana University Press: Indiana.
- Silver MD, Hudson RED, et al. 1975. Morphologic observations on heart valve prostheses made of fascia lata. *Journal of Cardiovascular Surgery*. 94: 360-366.
- Simo JC, Rifai MS, et al. 1990. On a stress resultant geometrically exact shell model. Part IV: variable thickness shells with through-the-thickness stretching. *Computer Methods in Applied Mechanics and Engineering*. 81: 91-126.
- Sodian R, Hoerstrup SP, et al. 2000. Early in vivo experience with tissue-engineered trileaflet heart valves. *Circulation*. 102: III22-III29.
- Sodian R, Hoerstrup SP, et al. 2000. Evaluation of biodegradable, three-dimensional matrices for tissue engineering of heart valves. *ASAIO Journal*. 46: 107-110.
- Spencer A.J.M. 1972. *Deformations of Fibre-Reinforced Materials*. Clarendon Press: Oxford.
- St. Jude Medical. [online] URL: <http://www.sjm.com/devices/devicetype> [cited May 25, 2005].
- Stark J, Bull C, et al. 1998. Fate of subpulmonary homograft conduits: determinants of late homograft failure. *Journal of Cardiovascular Surgery*. 115: 506-516.
- Sussman T., Bathe K.J. 1987. A finite-element formulation for nonlinear incompressible elastic and inelastic analysis. *Computers & Structures*. 26(1-2): 357-409.
- Sze KY, Zheng SJ, et al. 2004. A stabilized eighteen-node solid element for hyperelastic analysis of shells. *Finite Elements in Analysis and Design*. 40: 319-340.
- Tong P and Fung YC. 1974. The stress-strain relationship for the skin. *Journal of Biomechanics*. 7(1): 649-57.
- Vesely I, Boughner D. 1989. Analysis of the bending behavior of porcine xenograft

- leaflets and of natural aortic valve material: bending stiffness, neutral axis and shear measurements. *Journal of Biomechanics*. 22(6/7): 655-671.
- Vesely I, Noseworthy R. 1992. Micromechanics of the fibrosa and the ventricularis in aortic valve leaflets. *Journal of Biomechanics*. 25(1): 101-13.
- Vito R.P., Dixon S.A. 2003. Blood vessel constitutive models- 1995-2002. *Annual Review of Biomedical Engineering*. 5: 413-39.
- Votta E, Maisano F, Soncini M, et al. 2002. 3-D computational analysis of the stress distribution on the leaflets after edge-to-edge repair of mitral regurgitation. *Journal of Heart Valve Disease*. 11(6): 810-822.
- Vyahare NR, Chen W, et al. 1997. Current progress in anticalcification for bioprosthetic and polymeric heart valves. *Cardiovascular Pathology*. 6: 219-229.
- Weiss JA, Maker BN, and et al. 1996. Finite element implementation of incompressible, transversely isotropic hyperelasticity. *Computer Methods in Applied Mechanics and Engineering*. 135: 107-28.
- Weiss J., Maker B., Govindjee S. 1996. Finite element implementation of incompressible, transversely isotropic hyperelasticity. *Computer Methods in Applied Mechanics and Engineering* 135, 107-28.

Appendix A: Derivation of all terms for mixed pressure-displacement formulation

The original strain energy function is

$$W(I_1, I_4) = c_0 \left\{ \exp \left[c_1 (I_1 - 3)^2 + c_2 (I_4^{1/2} - 1)^4 \right] - 1 \right\} \quad (\text{A.1})$$

In the mixed formulation, a term is added including the interpolated pressure and pressure calculated from the displacements,

$$Q = -\frac{1}{2} (\bar{p} - \tilde{p})^2, \quad (\text{A.2})$$

and the pressure is calculated from the displacements by

$$\bar{p} = -\kappa (I_3 - 1). \quad (\text{A.3})$$

We also include a term to ensure positive definiteness of the constitutive tensor at low strains,

$$W^{(PD)}(I_1) = c_{PD} (I_1 - 3). \quad (\text{A.4})$$

The invariants of the right Cauchy-Green strain that are used are

$$\begin{aligned} I_1 &= \text{tr} \mathbf{C}, \\ I_3 &= \det \mathbf{C}, \\ I_4 &= \mathbf{N} \cdot \mathbf{C} \cdot \mathbf{N}. \end{aligned} \quad (\text{A.5})$$

Modified invariants are defined to make I_1 and I_4 independent of volume changes, and to make I_3 equal exactly the volume ratio,

$$\begin{aligned} J_1 &= I_1 I_3^{-1/3}, \\ J_3 &= \sqrt{I_3}, \\ J_4 &= I_4 I_3^{-1/3}. \end{aligned} \quad (\text{A.6})$$

The complete strain energy function with modified invariants is

$$W(J_1, J_4) = c_0 \left\{ \exp \left[c_1 (J_1 - 3)^2 + c_2 (J_4^{1/2} - 1)^4 \right] - 1 \right\} - \frac{1}{2} (\bar{p} - \tilde{p})^2 + c_{PD} (J_1 - 3). \quad (\text{A.7})$$

We need to calculate the second Piola-Kirchoff stresses

$$\mathbf{S} = 2 \frac{\partial W}{\partial \mathbf{C}}, \quad (\text{A.8})$$

and the constitutive tensor

$$\mathbf{C} = 4 \frac{\partial^2 W}{\partial \mathbf{C}^2}. \quad (\text{A.9})$$

We need to calculate a number of derivative terms. We will use the notation

$$(\circ)_{ij}^* = \frac{\partial (\circ)_i}{\partial \mathbf{C}_j} + \frac{\partial (\circ)_j}{\partial \mathbf{C}_i}. \quad (\text{A.10})$$

1. Derivatives of modified invariants w.r.t. invariants

$$\begin{aligned} \frac{\partial J_1}{\partial I_1} &= I_3^{-1/3} \\ \frac{\partial J_1}{\partial I_3} &= -\frac{1}{3} I_1 I_3^{-4/3} \\ \frac{\partial J_3}{\partial I_3} &= \frac{1}{2} I_3^{-1/2} \\ \frac{\partial J_4}{\partial I_3} &= -\frac{1}{3} I_4 I_3^{-4/3} \\ \frac{\partial J_4}{\partial I_4} &= I_3^{-1/3} \end{aligned} \quad (\text{A.11})$$

2. Second derivatives of modified invariants w.r.t. invariants

$$\begin{aligned} \frac{\partial^2 J_1}{\partial I_1 \partial I_3} &= -\frac{1}{3} I_3^{-4/3} \\ \frac{\partial^2 J_1}{\partial I_3^2} &= \frac{4}{9} I_1 I_3^{-7/3} \\ \frac{\partial^2 J_3}{\partial I_3^2} &= -\frac{1}{4} I_3^{-3/2} \\ \frac{\partial^2 J_4}{\partial I_3^2} &= \frac{4}{9} I_4 I_3^{-7/3} \\ \frac{\partial^2 J_4}{\partial I_3 \partial I_4} &= -\frac{1}{3} I_3^{-4/3} \end{aligned} \quad (\text{A.12})$$

3. Derivatives of invariants w.r.t. strain

$$\begin{aligned}
 (I_1)_{ij}^* &= 2\delta \\
 (I_3)_{ij}^* &= 2C^{-1} \det C \\
 (I_4)_{ij}^* &= 2N \otimes N
 \end{aligned} \tag{A.13}$$

4. Derivatives of modified invariants w.r.t. strain

$$\begin{aligned}
 (J_1)_{ij}^* &= \frac{\partial J_1}{\partial I_1} (I_1)_{ij}^* + \frac{\partial J_1}{\partial I_3} (I_3)_{ij}^* \\
 (J_3)_{ij}^* &= \frac{\partial J_3}{\partial I_3} (I_3)_{ij}^* \\
 (J_4)_{ij}^* &= \frac{\partial J_4}{\partial I_3} (I_3)_{ij}^* + \frac{\partial J_4}{\partial I_4} (I_4)_{ij}^*
 \end{aligned} \tag{A.14}$$

5. Second derivatives of modified invariants w.r.t. invariants and strain

$$\begin{aligned}
 \left(\frac{\partial J_1}{\partial I_1} \right)_{ij}^* &= \frac{\partial^2 J_1}{\partial I_1 \partial I_3} (I_3)_{ij}^* \\
 \left(\frac{\partial J_1}{\partial I_3} \right)_{ij}^* &= \frac{\partial^2 J_1}{\partial I_1 \partial I_3} (I_1)_{ij}^* + \frac{\partial^2 J_1}{\partial I_3^2} (I_3)_{ij}^* \\
 \left(\frac{\partial J_3}{\partial I_3} \right)_{ij}^* &= \frac{\partial^2 J_3}{\partial I_3^2} (I_3)_{ij}^* \\
 \left(\frac{\partial J_4}{\partial I_3} \right)_{ij}^* &= \frac{\partial^2 J_4}{\partial I_3^2} (I_3)_{ij}^* + \frac{\partial^2 J_4}{\partial I_3 \partial I_4} (I_4)_{ij}^* \\
 \left(\frac{\partial J_4}{\partial I_4} \right)_{ij}^* &= \frac{\partial^2 J_4}{\partial I_3 \partial I_4} (I_3)_{ij}^*
 \end{aligned} \tag{A.15}$$

6. Second derivatives of invariants w.r.t strain

$$\begin{aligned}
 (I_1)_{ijrs}^{**} &= 0 \\
 (I_3)_{ijrs}^{**} &= [\hat{\epsilon}_{irc} \hat{\epsilon}_{jsf} + \hat{\epsilon}_{isc} \hat{\epsilon}_{jrf} + \hat{\epsilon}_{jrc} \hat{\epsilon}_{isf} + \hat{\epsilon}_{jsc} \hat{\epsilon}_{isf}] C_{cf} \\
 (I_4)_{ijrs}^{**} &= 0
 \end{aligned} \tag{A.16}$$

7. Second derivatives of modified invariants w.r.t strain

$$\begin{aligned}
(J_1)_{ijrs}^{**} &= \left(\frac{\partial J_1}{\partial I_1} \right)_{rs}^* (I_1)_{ij}^* + \left(\frac{\partial J_1}{\partial I_3} \right)_{rs}^* (I_3)_{ij}^* + \frac{\partial J_1}{\partial I_3} (I_3)_{ijrs}^{**} \\
(J_3)_{ijrs}^{**} &= \left(\frac{\partial J_3}{\partial I_3} \right)_{rs}^* (I_3)_{ij}^* + \frac{\partial J_3}{\partial I_3} (I_3)_{ijrs}^{**} \\
(J_4)_{ijrs}^{**} &= \left(\frac{\partial J_4}{\partial I_3} \right)_{rs}^* (I_3)_{ij}^* + \frac{\partial J_4}{\partial I_3} (I_3)_{ijrs}^{**} + \left(\frac{\partial J_4}{\partial I_4} \right)_{rs}^*
\end{aligned} \tag{A.17}$$

Derivatives of the complete strain energy function (Equation A.1) with respect to the modified invariants will be required. Using the notation,

$$W_n = \frac{\partial W}{\partial J_n}, W_{mn} = \frac{\partial^2 W}{\partial J_m \partial J_n}, \tag{A.18}$$

we have

$$\begin{aligned}
W_1 &= 2c_0 c_1 (J_1 - 3) \exp \left[c_1 (J_1 - 3)^2 + c_2 (J_4^{1/2} - 1)^4 \right] \\
W_4 &= 2c_0 c_2 (J_4^{1/2} - 1)^3 J_4^{-1/2} \exp \left[c_1 (J_1 - 3)^2 + c_2 (J_4^{1/2} - 1)^4 \right]
\end{aligned} \tag{A.19}$$

and

$$\begin{aligned}
W_{11} &= c_0 [2c_1 + 4c_1^2 (J_1 - 3)^2] \exp \left[c_1 (J_1 - 3)^2 + c_2 (J_4 - 1)^4 \right] \\
W_{14} &= 4c_0 c_1 c_2 (J_1 - 3) (J_4^{1/2} - 1)^3 J_4^{-1/2} \exp \left[c_1 (J_1 - 3)^2 + c_2 (J_4 - 1)^4 \right] \\
W_{44} &= \left[3c_0 c_2 (J_4^{1/2} - 1)^2 J_4^{-1} - c_0 c_2 (J_4^{1/2} - 1)^3 J_4^{-3/2} + 4c_0 c_2^2 (J_4^{1/2} - 1)^6 J_4^{-1} \right] \\
&\quad * \exp \left[c_1 (J_1 - 3)^2 + c_2 (J_4 - 1)^4 \right]
\end{aligned} \tag{A.20}$$

The 2nd Piola Kirchoff stress tensor is

$$S_{ij} = \left(\tilde{W} \right)_{ij}^*, \tag{A.21}$$

which is found by taking the derivative of each term,

$$\begin{aligned}
S_{ij} &= \left(W^{(D)}\right)_{ij}^* + \left(W^{(V)}\right)_{ij}^* + \left(W^{(PD)}\right)_{ij}^*, \\
\left(W^{(D)}\right)_{ij}^* &= W_1 (J_1)_{ij}^* + W_4 (J_4)_{ij}^*, \\
\left(W^{(V)}\right)_{ij}^* &= k (J_3 - 1) (J_3)_{ij}^*, \\
\left(W^{(PD)}\right)_{ij}^* &= c_{PD} (J_1)_{ij}^*, \\
S_{ij} &= (W_1 + c_{PD}) (J_1)_{ij}^* + W_4 (J_4)_{ij}^* + k (J_3 - 1) (J_3)_{ij}^*,
\end{aligned} \tag{A.22}$$

where the derivatives are given above.

The constitutive tensor is

$$\mathbf{C}_{ijrs} = \left(S_{ij}\right)_{rs}^*. \tag{A.23}$$

Substituting with Equation A.22 gives

$$\begin{aligned}
E_{ijrs} &= \left(W^{(D)}\right)_{ijrs}^{**} + \left(W^{(V)}\right)_{ijrs}^{**} + \left(W^{(PD)}\right)_{ijrs}^{**} \\
\left(W^{(D)}\right)_{ijrs}^{**} &= \left(W_1 (J_1)_{ij}^* + W_4 (J_4)_{ij}^*\right)_{rs}^*, \\
\left(W^{(V)}\right)_{ijrs}^{**} &= \left(k (J_3 - 1) (J_3)_{ij}^*\right)_{rs}^*, \\
\left(W^{(PD)}\right)_{ijrs}^{**} &= \left(c_{PD} (J_1)_{ij}^*\right)_{rs}^*.
\end{aligned} \tag{A.24}$$

To evaluate \mathbf{C} , we define

$$\begin{aligned}
A_{ijrs} &= \left[W_1 (J_1)_{ij}^*\right]_{rs}^*, \\
B_{ijrs} &= \left[W_4 (J_4)_{ij}^*\right]_{rs}^*, \\
D_{ijrs} &= \left[k (J_3 - 1) (J_3)_{ij}^*\right]_{rs}^*, \\
E_{ijrs} &= \left[c_{PD} (J_1)_{ij}^*\right]_{rs}^*,
\end{aligned} \tag{A.25}$$

and apply the derivatives to find

$$\begin{aligned}
A_{ijrs} &= \left[W_{11} (J_1)_{rs}^* + W_{14} (J_4)_{rs}^* \right] (J_1)_{ij}^* + W_1 (J_1)_{ijrs}^{**}, \\
B_{ijrs} &= \left[W_{14} (J_1)_{rs}^* + W_{44} (J_4)_{rs}^* \right] (J_4)_{ij}^* + W_4 (J_4)_{ijrs}^{**}, \\
D_{ijrs} &= \kappa \left[(J_3)_{ij}^* (J_3)_{rs}^* + (J_3 - 1) (J_3)_{ijrs}^{**} \right], \\
E_{ijrs} &= c_{PD} (J_1)_{ijrs}^{**}.
\end{aligned} \tag{A.26}$$

All derivatives are given above, and then the constitutive tensor is calculated by

$$\mathbf{C}_{ijrs} = A_{ijrs} + B_{ijrs} + D_{ijrs} + E_{ijrs}. \tag{A.27}$$

The equations given here are sufficient to completely define the response based on the given strain-energy function (Equation A.1) for finite element analysis.